

# **Infragravity wave behaviour in a secondary tidal inlet, at the Slufter, the Netherlands**



J.J. de Vries  
2<sup>nd</sup> version MSc thesis  
04-03-2010

Supervisors:  
Dr. B.G. Ruessink  
Dr. M. van der Vegt

Physical Geography  
Utrecht University

## **Preface**

All knowledge obtained during my bachelor Earth Sciences and master Physical Geography at Utrecht University is united into this final MSc product, my master thesis. It is with great pleasure that I studied at Utrecht University for five year. The fieldwork at the Slufter and the entire Master's program, was a very educative and positive experience for me. I would like to thank the coastal group of Utrecht University, Prof. Dr. P. Hoekstra, Dr. M. van der Vegt and Dr. B.G. Ruessink, for the well structured and open way of supervision they offered during the fieldwork and during the entire program. I would also like to thank Dr. B.G. Ruessink for the helpful discussions and positive criticism, while supervising me during the process of writing my MSc thesis. Furthermore, the technicians of Utrecht University, H. Markies, C. Roosendaal and M. van Maarseveen, are greatly appreciated for all their help during the fieldwork on Texel. Without their help, the fieldwork would not have worked out. Of course, the fieldwork would never have worked out so well either without the good cooperation and nice relaxing time with my fellow MSc-students at the Slufter, Nynke Vellinga, Marjolijn Witteveen and Hans Brockhus. Furthermore, I'd like to thank my parents, Nico and Coby and my girlfriend Ronja for their never ending interest and their support during my Bachelor's and Master's program.

# Table of contents

Table of contents .....	2
List of figures.....	3
List of tables .....	5
Summary.....	6
1. Introduction .....	7
1.1 Motivation .....	7
1.2 Brief literature review.....	8
1.3 Research questions .....	13
1.4 Thesis outline.....	15
2. The 2009 Slufter campaign.....	16
2.1 Field site .....	16
2.2 Boundary conditions.....	17
2.3 Measurement transect.....	19
2.4 Data processing.....	26
3. Entire field campaign.....	29
3.1 Wave characteristics .....	29
3.2 Skewness and asymmetry.....	35
3.3 Conclusion nearshore wave characteristics .....	37
4. Infragravity wave behaviour during low- and high-energetic conditions .....	39
4.1 Characteristics of tidal cycles .....	39
4.2 Relative contribution low- and high-frequency waves during low- and high-energetic conditions.....	45
4.3 Spectral analysis .....	49
4.4 Phase difference analysis.....	51
4.5 Energy fluxes.....	55
5. Discussion: Dissipation mechanisms.....	59
6. Conclusion .....	64
References .....	66

## List of figures

Figure 1: Generation of a bound long wave due to a gradient in radiation stresses in wave groups. Black line is a propagating wave, blue line is bound long wave, dashed black line is still water level. The plus and minus refer to the relative magnitude of radiation stresses, where at a plus the radiation stress is high and at a minus radiations stress is low. ....	9
Figure 2: Time-varying breakpoint mechanism for a given slope. 3a) shows the wave height, 3b) shows the set up through the surf zone. $x'_1$ and $x'_2$ are the minimum and maximum position of the breakpoint, respectively (Symonds et al., 1982). ....	9
Figure 3: Progressive (a & c) and standing (b & d) wave pattern. a and b: water level fluctuation versus distance; c and d: water level or current velocity versus time (Masselink & Hughes, 2003). ....	10
Figure 4: Predicted (dashed line) and observed (solid line) cross-shore current (a) and elevation (b) spectra, coherence and phase at various depths (h) and average offshore distances (x) at Santa Barbara. Coherence and phase are with the run-up sensor (Guza & Thornton, 1985). ....	12
Figure 5: Overview of the Slufter (GoogleEarth). ....	16
Figure 6: Offshore boundary conditions during measurement campaign, in 2009: a) Offshore wave height, b) Offshore wave period, c) Offshore wave direction, d) Offshore water level fluctuation, e) Astronomic water level fluctuation and f) Surge. ....	17
Figure 7: Slufter hinterland on September 21 (a) and on October 4 (b) (J.J. de Vries) .....	18
Figure 8: Small and large tripod (J.J. de Vries). ....	20
Figure 9: Location of measurement instruments and median grain size along beach profile on September 19, 2009. ....	21
Figure 10: Digital Elevation Models of the Slufter inlet area: a) At start of measurement campaign (September 20), b) 4 days after the major storm event (October 8) and c) at the end of the field campaign (October 30). ....	24
Figure 11: a) 2-weekly morphological development of measurement transect, b) Impact storm on morphological development of the measurement transect. ....	25
Figure 12: Significant wave height ( $H_{m0}$ ) for each tripod measurement location: a) $H_{m0}$ (hf) ( $f [0.05-1]$ ), b) $H_{m0}$ (lf) ( $f [0.005-0.05]$ ), c) ratio between $H_{m0}$ (lf)/ $H_{m0}$ (hf), d) Offshore water level fluctuations. ....	29
Figure 13: Correlation between $H_{m0}$ Offshore (m) and $H_{m0}$ (lf) (m) per tripod location. ....	30
Figure 14: $H_{m0}$ at each measurement location between Julian day 269 and 272. a) $H_{m0}$ (hf), b) $H_{m0}$ (lf), c) ratio between $H_{m0}$ (lf) and $H_{m0}$ (hf). ....	30
Figure 15: Ratio between $H_{m0}$ (hf) and $H_{m0}$ (lf) for the different hydrodynamic zones. ....	33
Figure 16: a) Wave angle and b) wave spread of all tripods locations during the field campaign. ....	34
Figure 17: Skewness and asymmetry of all measurement locations against $H_{m0}/h$ : a) velocity skewness of high-frequency range, b) velocity skewness of low-frequency range, c) velocity asymmetry of high-frequency range, d) velocity asymmetry of low-frequency range. ....	36
Figure 18: Skewness and asymmetry of all measurement locations against time: a) velocity skewness of high-frequency range, b) velocity skewness of low-frequency range, c) velocity asymmetry of high-frequency range, d) velocity asymmetry of low-frequency range. ....	37
Figure 19: Profile of the beachplain during low- and high-energetic conditions on October 7 (a) and before the high-energetic conditions of October 4 on September 29 (b) respectively. $x=0$ is 3 m seaward of LT. Measurement locations are indicated with the open dots from the seaward to the landward side measurement locations are: LT, ST1, ST2, ST3 and ST1-storm.	

Pressure sensors are the cross-symbols, from the seaward side across the beachplain: OSSI 1, OSSI 2, OSSI 3, OSSI 4, OSSI 5.....	40
Figure 20: 20 minute-averaged water depth and standard deviation of analyzed tidal cycles for (a) low-energetic conditions and (b) high-energetic conditions.....	41
Figure 21: 20 minute-averaged cross-shore (u) and alongshore (v) and its standard deviation for analyzed tidal cycles: a) u-mean during low-energetic conditions, b) u-std during low-energetic conditions,.....	43
Figure 22: Cross- and alongshore velocities during high- and low-energetic conditions: a) $u_{rms}$ , b) $v_{rms}$ , c) ratio $u_{rms}^2/v_{rms}^2$ , d) bed profile and location measurement profiles in hydrodynamic zones during low-energetic conditions (sh: shoaling, su: surf and sw: swash zone). e) $u_{rms}$ , f) $v_{rms}$ , g) ratio $u_{rms}^2/v_{rms}^2$ , h) bed profile and location measurement profiles in hydrodynamic zones during high-energetic conditions.....	44
Figure 23: Wave characteristics of low- and high-frequency ranges: a) $H_{m0}$ , b) ratio $H_{m0}(lf)/H_{m0}(hf)$ , c) $u_{rms}$ , d) Skewness, e) Asymmetry, f) bed profile and measurement locations during low-energetic conditions (sh: shoaling, su: surf, sw: swash zone and dry). : g) $H_{m0}$ , h) ratio $H_{m0}(lf)/H_{m0}(hf)$ , i) $u_{rms}$ , j) Skewness, k) Asymmetry, l) bed profile and measurement locations during high-energetic conditions.....	45
Figure 24: Spectral densities of the total frequency range (a) and of the low-frequency range (b) during low-energetic conditions and bed profile and measurement locations (c). Spectral densities of the total frequency range (d), of the low-frequency range (e) during high-energetic conditions and bed profile and measurement locations (f). .....	49
Figure 25: Phase differences (a), predicted phase differences (b) and coherence (c) of total frequency range during low-energetic conditions. Phase differences (d), predicted phase differences (e) and coherence (f) of low-frequency range during low-energetic conditions. Phase differences (h), predicted phase differences (i) and coherence (j) of total frequency range during high-energetic conditions. Phase differences (k), predicted phase differences (l) and coherence (m) of low-frequency range during high-energetic conditions. Beach profile and measurement locations during low- (g) and high-energetic conditions (n). .....	52
Figure 26: Bulk onshore (a) and offshore (b) high-frequency energy fluxes (0.05-0.4 Hz) and (c) bulk high-frequency reflection coefficient during low-energetic conditions and d) bed profile and measurement locations. Bulk onshore (e) and offshore (f) high-frequency energy fluxes and (g) bulk high-frequency reflection coefficient during high-energetic conditions and h) bed profile and measurement locations.....	55
Figure 27: Bulk onshore (a) and offshore (b) infragravity energy fluxes (0.005-0.05 Hz) and (c) bulk infragravity reflection coefficient during low-energetic conditions and d) bed profile and measurement locations. Bulk onshore (e) and offshore (f) infragravity energy fluxes (0.005-0.05 Hz) and (g) bulk infragravity reflection coefficient during high-energetic conditions and h) bed profile and measurement locations. ....	56
Figure 28: Bulk northward-, $F^+$ , (a) and southward-directed, $F^-$ , (b) low- and high-frequency energy fluxes (0.005-0.05 Hz, 0.05-0.4 Hz) and (c) bulk infragravity reflection coefficient during low-energetic conditions and d) bed profile and measurement locations. Bulk northward-, $F^+$ , (e) and southward-directed, $F^-$ , (f) low- and high-frequency energy fluxes and (g) bulk infragravity reflection coefficient during high-energetic conditions and h) bed profile and measurement locations.....	58
Figure 29: a) measured and modelled $H_{rms,fr}$ , b) $D_{bot}$ and $D_{br}$ , c) the ratio of $D_{br}/D_{bot}$ of each frequency range during low-energetic conditions. e) measured and modelled $H_{rms,fr}$ , f) $D_{bot}$ and $D_{br}$ , g) the ratio of $D_{br}/D_{bot}$ of each frequency range during high-energetic conditions. d) and h) bed profile and measurement locations during low- and high-energetic conditions respectively.....	62

**List of tables**

Table 1: Height above the bed ( $h_{ab}$  in cm) of all measurement devices at each measurement location. .... 22

Table 2: Residence times (in %). .... 32

Table 3: mean and variance of the ratio  $H_{m0}(lf)/H_{m0}(hf)$  for each hydrodynamic zone..... 33

Table 4:  $H_{m0}(hf)$  at each measurement location and the relative wave height of the hydrodynamic boundaries of each measurement location during low- and high-energetic conditions ( $H_{m0}(hf)/h$  values for boundary shoaling and surf zone,  $H_{m0}(hf)/h$  values for boundary surf and swash zone). .... 42

Table 5: frequency range (Hz), radial wave period (s) of each frequency range, range of representative shoaling depth (m) of each frequency range and normalized bed slope of each frequency range during low- and high-energetic conditions. Slope during low- and high-energetic conditions is 0.0155 and -0.0033 respectively..... 60

## Summary

In Autumn 2009, a field campaign was done in a secondary tidal inlet called the Slufter, located on the most southern Wadden island Texel, the Netherlands. A general definition of a Slufter, or secondary tidal inlet, is a salt or brackish dune valley, which is connected with the open sea and is flooded completely at least once a year. The aim of this research was to better understand infragravity wave behaviour at the Slufter during different energetic conditions and to investigate the influence of the supratidal beachplain on infragravity wave behaviour. The research is part of a larger research to better understand hydro- and morphodynamics of secondary tidal inlets.

Infragravity, or low-frequency, wave height at the Slufter is related to offshore wave height and water depth. Low-frequency wave height remains constant in the shoaling and surf zone, whereas high-frequency wave height decreases. Low-frequency waves become more dominant over high-frequency waves in the inner surf and swash zone during normal, low-energetic, beach conditions. Low-frequency waves become increasingly skewed and asymmetric in the swash zone and break close to the. Low-frequency wave dissipation is caused by bed friction and low-frequency wave breaking and results in a cross-shore progressive infragravity wave pattern during low-energetic conditions, which contrasts with findings from other studies.

During a storm event, the supratidal beachplain is flooded and low-frequency waves propagate over the beachplain. Low-frequency waves are dominant over high-frequency waves on top of the beachplain. However, the ratio is smaller than during normal beach conditions. Low-frequency waves become skewed and asymmetric while propagating over the beachplain, but do not break. During high-energetic conditions, low-frequency wave dissipation occurs at the landward side of the beachplain due to bed friction. Observations suggest that high-frequency wave-induced turbulence may also significantly contribute to low-frequency wave dissipation.

# 1. Introduction

In this chapter an introduction to the research is given. In section 1.1 the motivation and relevance for this study is discussed. In section 1.2 a brief literature overview about infragravity waves is given. Based on the literature overview, research questions for this research are formulated in section 1.3. In section 1.4, the thesis outline is presented.

## 1.1 Motivation

In this thesis, the behaviour of infragravity waves at a secondary tidal inlet, the Slufter, the Netherlands, is treated. Infragravity, or low-frequency, waves, are waves with a significantly lower frequency than wind-driven high-frequency waves (Guza & Thornton, 1985) and have been studied extensively during the last decades due to their importance to sediment transport in the nearshore area (Guza & Thornton, 1985; Masselink 1995; Karunarathna & Chadwick, 2007 and many others). Contrary to the wave height of high-frequency waves, low-frequency wave height, and with it infragravity wave energy, does not diminish towards the shore, but increases onshore (Guza&Thornton, 1985; Ruessink, 1998a; Karunarathna & Chadwick, 2007). Therefore, infragravity waves influence sediment transport patterns in the nearshore. Many studies on infragravity waves were performed in controlled environments or with modelling (Madsen et al., 1997, Baldock et al, 2000). Therefore much is unknown about infragravity wave behaviour under natural circumstances (Herbers et al., 1995; Elfrink & Baldock, 2002) and no research has been done on infragravity wave behaviour in secondary tidal inlets as the Slufter. The Slufter is a salt brackish dune valley, which is connected with the open sea by a tidal channel and is flooded completely at least once a year during a severe storm with its associated surge. Hydrodynamic processes may be very different between moderate and storm conditions. This thesis gives an insight in infragravity wave behaviour in a secondary tidal inlet under different energetic conditions.

This study is done as a part of the Master research program of 2009-2010 of the track Coastal Dynamics, Fluvial Systems and Climate Change of the master Physical Geography at Utrecht University. The goals of the Master research and Master thesis are to learn how to independently plan and execute a field work and how to write a good scientific report. Furthermore, all knowledge obtained during the Master program Physical Geography is integrated into this final product. The MSc-research project at the Slufter is part of a larger research project focused on better understanding the morpho- and hydrodynamic behaviour of secondary tidal inlets.

## 1.2 Brief literature review

Research of the past decades on infragravity waves has pointed out that infragravity waves play an important role in the nearshore area. In this section a review of the research of the past decades on infragravity waves in the nearshore is given. This literature overview is a short summary from a report written as a preparation for this research.

Infragravity waves are defined as waves with a frequency between 0.005 Hz and 0.05 Hz (Aagaard & Bryan, 2003; Henderson & Bowen, 2003) or with a frequency between 0.004 Hz and 0.04 Hz (Herbers et al., 1995; Ruessink, 1998b). The choice of the upper frequency limit is slightly arbitrary, but is based on the lowest frequency that may possibly contain significant amounts of energy incident from deep water (Guza & Thornton, 1985). Two mechanisms for the generation of infragravity waves have been proposed. Longuet-Higgins & Stewart (1962) proposed that bound infragravity waves are generated due to a gradient in radiation stress in wave groups. When a high-frequency wave field consists of two or more different wave frequencies, wave grouping occurs. Longuet-Higgins & Stewart (1962) demonstrated that small second-order undulations accompany a first-order wave group due to difference in radiation stresses in a wave group. Equation 1 is to compute the cross-shore radiation stress (Masselink & Hughes, 2003)

$$S_{xx} = \frac{2}{3}E = \frac{3}{16}\rho gH^2, \quad (1)$$

where  $S_{xx}$  is the cross-shore component of the radiation stress ( $N/m^2$ ) for waves approaching the beach with their crest parallel to the shoreline,  $E$  is the wave energy (J) proportional to 1/8 times the density of water ( $\rho=1000-1030 \text{ kg/m}^3$ ), the gravitational acceleration ( $g=9.81 \text{ m/s}^2$ ) and the wave height ( $H$  in meters)

Large waves have a larger mass transport than small waves and the difference in momentum flux and radiations stresses cause fluid to be expelled from groups of high waves to groups of low waves (Masselink, 1995). This leads to a set-down of the water level underneath the high waves and a set-up of the water level underneath the small waves, as is shown in figure 1. A long wave bound to the wave group is present, which is 180 degrees out of phase with the wave group and has an amplitude positively related to the wave groupiness (List, 1991; Madsen et al., 1997) and the incident wave height (Masselink, 1995; Raubenheimer et al., 1996; Ruessink, 1998a). The bound infragravity wave is released during wave breaking even though the exact mechanism is not known.

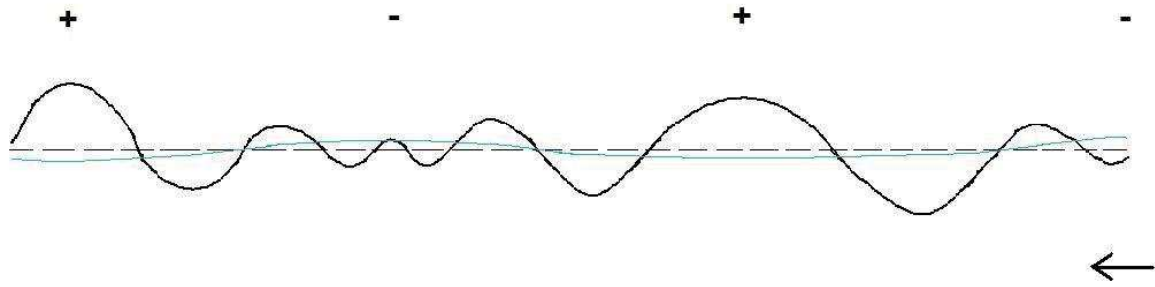


Figure 1: Generation of a bound long wave due to a gradient in radiation stresses in wave groups. Black line is a propagating wave, blue line is bound long wave, dashed black line is still water level. The plus and minus refer to the relative magnitude of radiation stresses, where at a plus the radiation stress is high and at a minus radiations stress is low.

Symonds et al. (1982) proposed a theory explaining the generation of infragravity waves by a time varying breakpoint as shown in figure 2, where a horizontal shift of the breakpoint due to wave groupiness results in a change in radiation stress, resulting in a progressive offshore directed wave seaward of the breakpoint and a standing wave landward of the breakpoint.

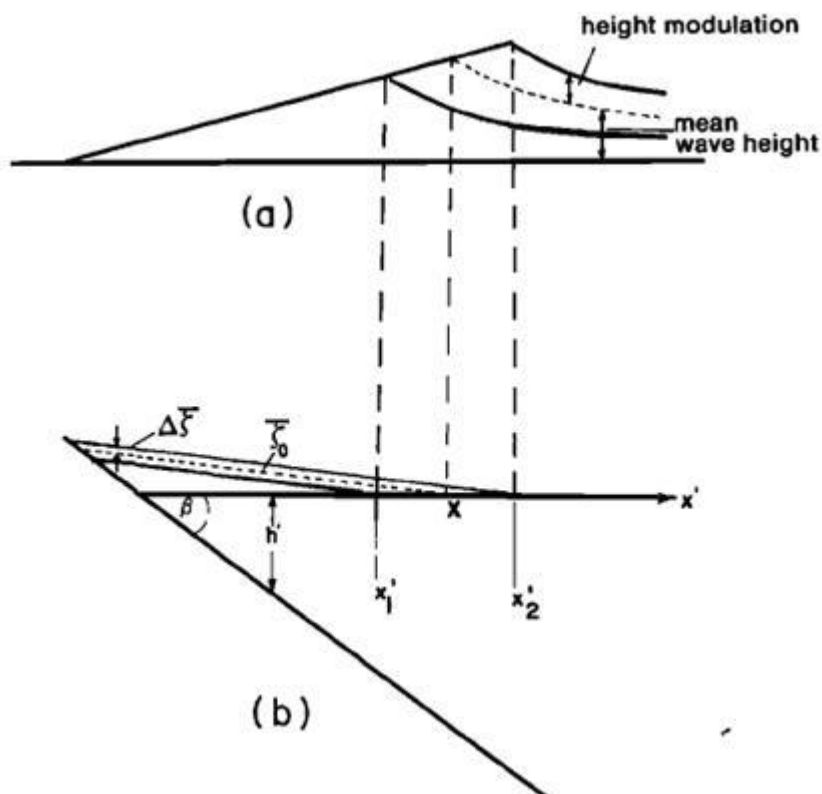


Figure 2: Time-varying breakpoint mechanism for a given slope. 3a) shows the wave height, 3b) shows the set up through the surf zone.  $x'_1$  and  $x'_2$  are the minimum and maximum position of the breakpoint, respectively (Symonds et al., 1982).

Both mechanisms may occur under natural conditions. The question that remains is which mechanism is dominant under natural conditions and under which surf zone conditions (Herbers et al., 1995; Madsen et al., 1997; Ruessink, 1998; Elfrink & Baldock, (2002).

Many laboratory and computer simulations and fewer field studies have been performed to determine the dominance of the one mechanism over the other. Baldock et al. (2000) and Karunarathna & Chadwick (2007) found a dominance of the time-varying breakpoint, whereas Ruessink (1998a & 1998b), Masselink (1995), Henderson et al. (2001) and Sheremet et al. (2002) found a dominance of infragravity generation by bound long waves over the time-varying breakpoint. Furthermore, Henderson et al. (2001) found a more progressive cross-shore infragravity wave pattern, whereas Baldock et al. (2000) found a more standing wave pattern, indicating a dominance of the time-varying breakpoint mechanism.

Furthermore, Raubenheimer (2002) found that the asymmetry and flow velocity of infragravity waves increase in the surf zone and reach a maximum in the outer swash zone, after which they decrease rapidly. The wave height remains constant over the entire surf zone and then rapidly decreases the swash zone. Butt & Russel (1999) found that infragravity waves are negatively skewed in the nearshore area during high-energetic conditions and become more negatively skewed towards the shoreline. However, the exact processes resulting in this increase in negative skewness are unknown.

Infragravity waves occur in standing or progressive form as shown in figure 3. The presence of a standing or progressive infragravity wave pattern depends on the phase coupling between the onshore-directed and offshore-directed infragravity wave (Elgar et al., 1997) and the magnitude of wave dissipation and reflection.

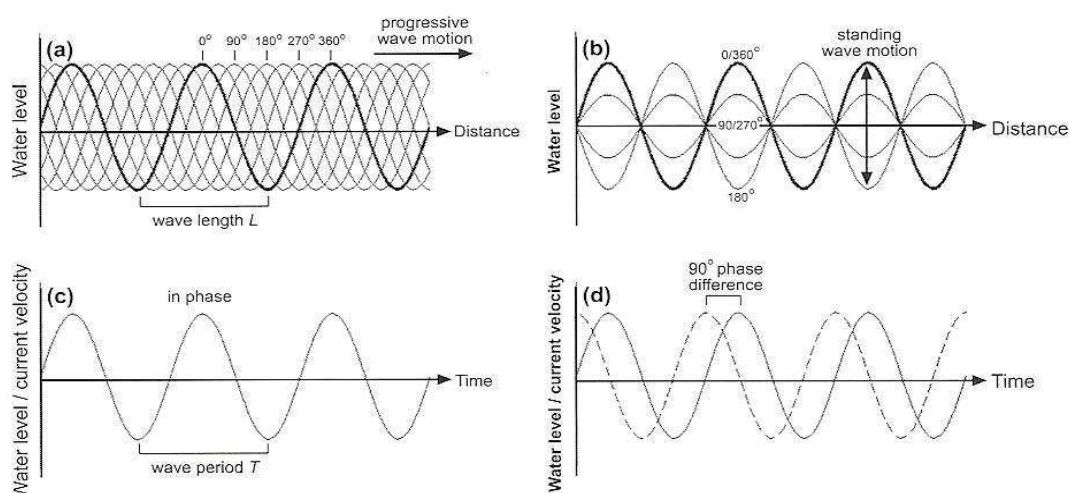


**Figure 3: Progressive (a & c) and standing (b & d) wave pattern. a and b: water level fluctuation versus distance; c and d: water level or current velocity versus time (Masselink & Hughes, 2003).**

Figure 4 shows the cross-shore infragravity wave pattern identified by Guza & Thornton (1985) based on the spectral density, phase difference and coherence between the most seaward measurement location and the run-up sensor. A cross-shore standing infragravity wave pattern can be distinguished by comparing maxima and minima in its spectral density. Maxima at a certain location from the shoreline will occur at the anti-node of the standing infragravity wave at a certain frequency, whereas minima represent nodes. A progressive pattern shows a less clear and periodical distinction between spectral maxima and minima.

The phase difference between two measurement locations is used to determine a standing infragravity wave and estimate the length of the standing wave. One measurement location located at an anti-node and one at a node have a phase difference of 90 degrees. Measurement locations close to each other have a phase difference close to zero. The frequency of abrupt changes in phase difference along the measurement transect is an indication of the amount of nodes and anti-nodes along the measurement transect and also for the wave length of a standing infragravity wave. For 2 measurement locations close to each other or far away, a progressive wave pattern has a gradual increasing phase difference with increasing frequency, since waves with a higher frequency have shorter wave lengths and will therefore have a larger phase difference while propagating onshore.

Coherence is near 1 for the cross-spectral analysis between the measurement locations if the locations correspond with a node or anti-node at a certain frequency and decreases if the locations do not correspond with a node or anti-node at a certain frequency. A progressive wave pattern has a more irregular fluctuating coherence. For more information on standing wave determination is referred to Bauer and Greenwood (1990).

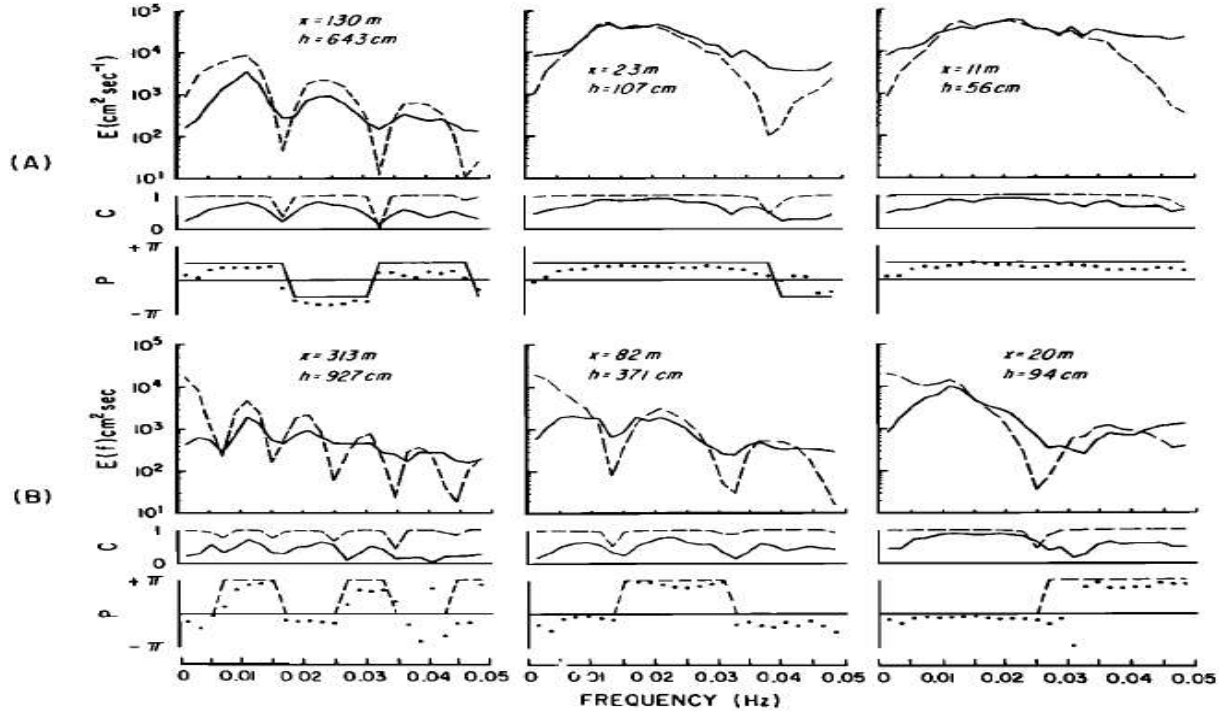


Figure 4: Predicted (dashed line) and observed (solid line) cross-shore current (a) and elevation (b) spectra, coherence and phase at various depths ( $h$ ) and average offshore distances ( $x$ ) at Santa Barbara. Coherence and phase are with the run-up sensor (Guza & Thornton, 1985).

A standing or progressive cross-shore infragravity wave pattern can also be determined by computing the onshore and offshore energy fluxes. Sheremet et al. (2002) calculated the shoreward ( $F^+$ ) and seaward ( $F^-$ ) infragravity energy fluxes with equation 2, assuming shore-normal wave propagation

$$F^\pm = \frac{\sqrt{gh}}{4} \int (PP + \frac{h}{g}UU \pm \sqrt{\frac{4h}{g}}PU)df, \quad (2)$$

where  $PP(f)$  and  $UU(f)$  are the auto-spectra of pressure and cross-shore velocity respectively,  $PU(f)$  is the cross-spectrum of pressure and cross-shore velocity, and the integral is over the infragravity frequency ( $f$ ).

Reflection of the infragravity waves at the shoreline is determined with  $R^2$  which is the ratio between  $F^-$  and  $F^+$ . Values vary between 0.5 and 4 (Elgar et al., (1994) & Herbers et al. (1995) in Sheremet et al. (2002)) and are divided into  $R^2$  values smaller and larger than 1, representing an energy sink and source respectively between the most seaward measurement location and the shoreline (Sheremet et al., 2002). The amount of reflection at the shoreline depends on the dissipation of the onshore-directed infragravity wave. Sheremet et al. (2002)

found that reflection was in the order of 0.2-0.8. Henderson et al. (2001) and Sheremet et al. (2002) found that infragravity waves only partially reflected against the shoreline, where Karunarathna & Chadwick (2007) found that reflection of infragravity waves at the shoreline is highest at lower group frequencies.

Infragravity wave dissipation has also been observed in the nearshore and has been ascribed to bed friction and wave breaking (Ruessink, 1998b; Sheremet et al., 2002; Henderson & Bowen, 2002; Battjes et al., 2004; van Dongeren et al., 2007)). Ruessink (1998b) and Thomson et al. (2006) found that during high-energetic conditions, the infragravity wave energy decreases from the surf zone towards the shoreline, which contrasts with findings of Guza & Thornton (1985) and Karunarathna & Chadwick (2007) who found an increase in infragravity wave energy, when offshore wave height increases. Henderson et al. (2006) and Thomson et al. (2006) found that the dominant process during low- and moderate-energetic conditions is nonlinear energy transfer in the surf zone to high-frequency waves. This contradicts with findings from van Dongeren et al. (2007) who found that wave breaking is the dominant dissipation mechanism on mild-sloped beaches. They found that locally the dissipation due to wave breaking is almost a factor 20 larger than dissipation due to bed friction.

Tides result in a lateral shift of hydrodynamic zones (Masselink et al., 2006; Price & Ruessink, 2008) resulting in a change of infragravity wave behaviour at a fixed location. During a tidal cycle, fluctuations in cross-shore infragravity pattern, in the ratio between bound and free infragravity waves, in the bulk infragravity coefficient  $R^2$  and fluctuations in infragravity energy dissipation rates may occur, where beach bathymetry strongly influences infragravity energy dissipation.

### **1.3 Research questions**

The great number of studies done on infragravity propagation and transformation has led to a better understanding of infragravity wave behaviour in the nearshore, but since many studies have been performed under laboratory conditions or through computer simulations, the behaviour of infragravity waves under natural conditions is still not completely understood. The propagation and transformation of infragravity waves in a secondary tidal inlet, such as the Slufter, has not been investigated at all and many questions remain still on how infragravity waves propagate and transform in an environment sheltered from waves. Furthermore, the location of the beachplain in the Slufter has a significant impact on

infragravity wave propagation during more energetic conditions, where it is especially interesting how the beachplain affects the magnitude of reflection of infragravity waves during different weather conditions. Not much is known about dissipation of infragravity wave energy in a secondary tidal inlet either.

A better understanding of infragravity wave propagation and transformation will aid in understanding erosion and sedimentation processes in the Slufter and is required to understand short- and long-term evolution of the Slufter.

The Slufter is very dynamic and a large difference in inundation occurs during different tide and weather conditions. The hypothesis proposed is that the submergence of the supratidal beachplain during a storm will have important ramifications on infragravity wave behaviour in the Slufter. It is hypothesized that a cross-shore standing infragravity wave pattern is present under normal conditions, which will change in a cross-shore progressive infragravity wave pattern across the beachplain during a storm. In addition, infragravity waves across to beachplain are expected to be skewed and asymmetric. The research questions below are formulated to be able to test the hypothesis stated above:

- What is the wave height of infragravity waves in the Slufter as a function of water depth and under different energetic conditions on the beach and on the beachplain and what is their relative contribution in the nearshore compared to the entire wave spectrum?
- What is the infragravity wave skewness and asymmetry in the Slufter as a function of water depth and during different energetic conditions on the beach and on the beachplain?
- What is the cross-shore infragravity wave pattern in the Slufter as a function of water depth and during different energetic conditions on the beach and on the beach plain?
- What is the reflection rate of infragravity waves in the Slufter as a function of water depth and during different energetic conditions on the beach and on the beachplain and what is the influence of the beachplain on infragravity wave propagation and reflection at the Slufter?

## **1.4 Thesis outline**

In chapter 2, characteristics of the field campaign are discussed, including the morphodynamic behaviour of the field site, the measurement transect and the boundary conditions during the field work. Also, the methodology and data processing is discussed. In chapter 3, the infragravity wave behaviour during the entire field campaign and their relative contribution to high-frequency waves is analyzed. In chapter 4, the differences and similarities in infragravity wave behaviour during low- and high-energetic conditions is treated. In chapter 5, possible causes for infragravity wave dissipation are discussed and in chapter 6 the most important findings of this research are summarized.

## 2. The 2009 Slufter campaign

### 2.1 Field site

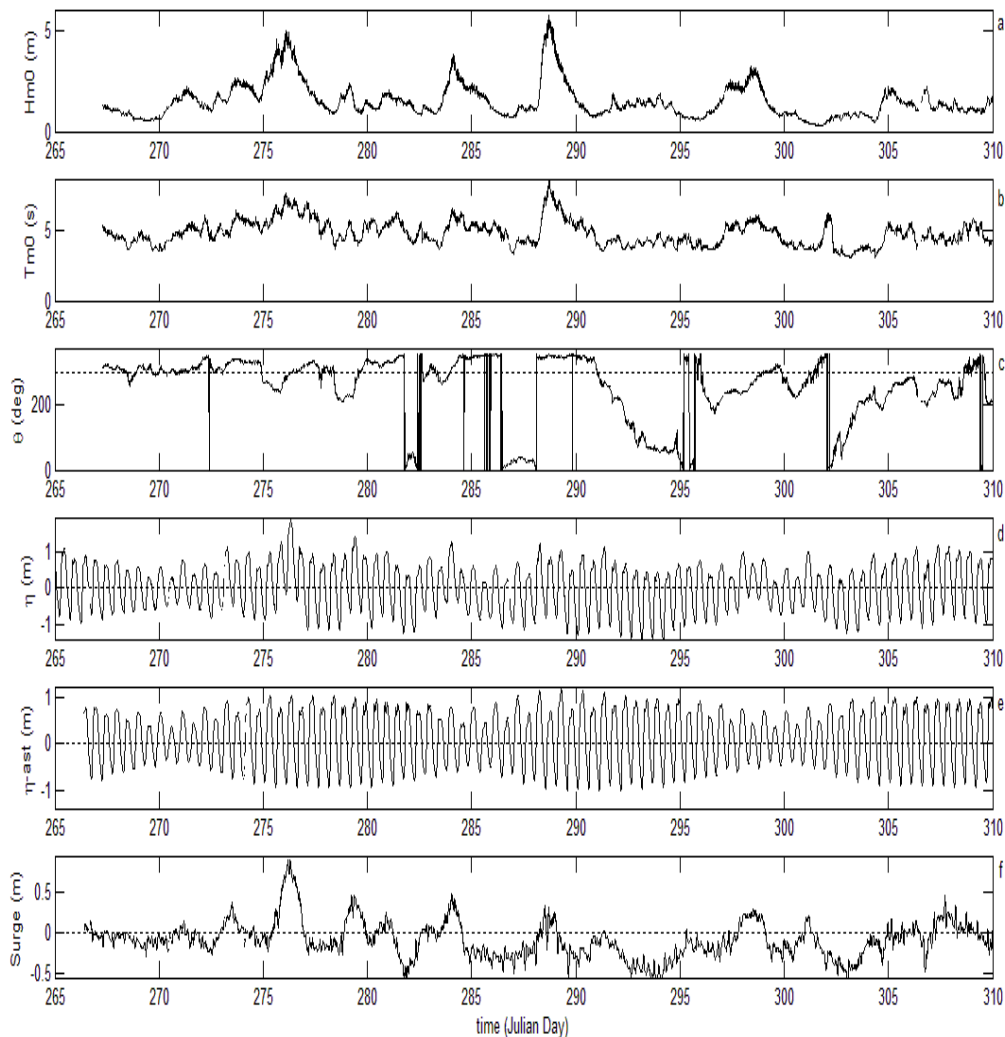
Figure 5 shows the Slufter at the Dutch barrier island of Texel. The Slufter is a secondary tidal inlet which is connected with the open sea by a tidal channel and is flooded completely at least once a year during a severe storm with its associated surge. Presently, the area of the Slufter spans approximately 1.62 km<sup>2</sup> of which 0.20 km<sup>2</sup> consist of dunes and dune valleys with an elevation +2 meters above mean sea level. 1.09 to 1.21 km<sup>2</sup> consist of slightly vegetated sand plains with an elevation between +0.8 and +1.0 meter above mean sea level. Approximately 0.32 km<sup>2</sup> are flooded diurnally (Durieux, 2004). The Slufter is flooded completely for floods larger than 1.7 meter above mean sea level which is expected to occur approximately 9 times per year. During such large floods, the beachplain, depicted in figure 5, is completely inundated and hydrodynamic processes at the Slufter may be very different from moderate weather conditions. Under moderate weather conditions, the beachplains lies dry and sediments are primarily transported by wind.



Figure 5: Overview of the Slufter (GoogleEarth).

## 2.2 Boundary conditions

The fieldwork at the Slufter was executed from September 17, 2009 until November 1, 2009, or from Julian day 259 until Julian day 304. The boundary conditions during the fieldwork are given in Figure 6. The significant wave height ( $H_{m0}$ ), the significant wave period ( $T_{m0}$ ) and the wave direction ( $\theta$ ) were measured by a buoy at the Eierlandse Gat, the tidal inlet between Texel and Vlieland, located approximately 20 km north of the Slufter in 26 m water depth. The measured and astronomical ( $\eta$  and  $\eta_{ast}$ ) were measured and computed from the tidal station 'Texel North Sea' 15 km south of the Slufter in approximately 20 m water depth. The surge level was computed by subtracting the astronomical from the actual water level fluctuations. The shore-normal is 300 degrees relative to the North.



**Figure 6: Offshore boundary conditions during measurement campaign, in 2009: a) Offshore wave height, b) Offshore wave period, c) Offshore wave direction, d) Offshore water level fluctuation, e) Astronomic water level fluctuation and f) Surge.**

Figure 6a shows 2 major storm events on October 4 and 16, Julian day 276 and 288, with  $H_{m0}$  up to 5 and 5.8 m respectively and 2 minor storm events on October 12 and 26, Julian day 284 and 298, with  $H_{m0}$  up to 3.8 and 3.2 m respectively.

During the storm event on October 4, on Julian day 276, the entire beachplain of the Slufter was flooded as was the hinterland (Figure 7). The storm event on October 16, on Julian day 288, resulted in partial inundation of the beachplain due to a smaller storm surge caused by a more north eastern wind direction, whereas the wind direction on October 4 was more southwest directed, resulting in a storm surge of more than 1 meter. Both events occurred during springtide.

The minor storm events on Julian days 284 and 298 did not result in complete inundation of the beachplain since the storms occurred during neap tide and because the storm surge was smaller than during the major storm events (Figure 6e&f). Under moderate weather conditions, the  $H_{m0}$  varied between 0.5 and 2.2 m.

The  $T_{m0}$  varied between 3 and 6 seconds under moderate weather conditions and was between 7 and 8.5 seconds during the 2 major storm events. Generally,  $\theta$  varied between southwest and northwest. During the 2 major storm events on Julian day 276 and 288,  $\theta$  was west-southwest and northwest respectively (Figure 6c).



**Figure 7: Slufter hinterland on September 21 (a) and on October 4 (b) (J.J. de Vries)**

## 2.3 Measurement transect

The measurements at the Slufter were done along a transect across the beachplain in the Slufter. Along the measurement transect, tripods (metal frames with measurement devices) and Ossi's (pressure sensors attached to metal poles) were located.

At the tripods, flow velocity was measured with an electromagnetic current meter (EMF) which measures flow velocity by creating a magnetic field, which is distorted by the flow. From the distortion the velocity is obtained. Flow velocity is measured in two directions, i.e. cross-shore (x) and alongshore direction (y). Onshore cross-shore velocities are defined as positive, where offshore cross-shore velocities are negative. The positive (negative) alongshore velocity is 90 degrees anti-clockwise of the positive (negative) cross-shore velocity.

Two different pressure sensors were used during the fieldwork. Five OSSIs (Ocean Sensor System Inc.) were used on different locations, whereas another four Keller pressure transducers were placed along with the EMF's at the tripods. Both sensors were used to obtain water level fluctuation data. Data output is in millivolt, but due to calibration with linear theory and subtraction of the air pressure, water level fluctuations are obtained. Air pressure was measured every 10 minutes during the field campaign.

The accuracy of the pressure sensors is  $\pm 0.25\%$  of the measured value (van Rijn, 2002). Errors in water depth and wave height derived from pressure sensors are caused by application of linear wave theory, variations of the water density, variations in the height of the sensor above the local bed and variations in barometric pressure (van Rijn et al., 2002). The largest error lies in determining the height of the pressure sensor above the bed (van Rijn et al., 2002). From a sensitivity analysis on the Coast3D-project, it is concluded that computed wave heights from pressure data has an accuracy of  $\pm 10\%$  (Ruessink (1999) in van Rijn, 2002).

Concluding, on each tripod one EMF, one pressure transducer, a floater and three sediment turbidity meters (STM), used for another MSc fieldwork, were attached to a data-logger. Small tripods started measuring after the floater was inundated. Measurements were performed continually with 4 Herz in burst of 15 minutes. The ST's were kept in place by lead weights, with a diameter of 5 cm, positioned on the legs of the frames. Furthermore, each ST was attached to a pole, buried more than 1 meter deep in the sand to prevent the ST's of washing away during severe storm events (Figure 8a). All ST's were orientated with the

measurement side seawards and orientated shore-parallel with an angle of 33 degrees relative to the North.

The LT was located seawards of the ST's and was equipped with more measurement devices relevant for another MSc-research on sediment transport and bedform migration. The relevant measurement devices at the Truc-Vert frame are two EMF's and one pressure transducer, which were also connected to a central data-logger measuring continually with 4 Hz in bursts of one tidal cycle. The LT was fixed in the sand by three poles (Figure 8b)

Pressure measurement with the OSSI's were done continually with 5 Hertz in bursts of 59 minutes per hour, after which no data is recorded for 1 minute. So a new burst starts every hour.



**Figure 8: Small and large tripod (J.J. de Vries).**

The measurement transect is depicted in figure 9. The seaward boundary of the measurement transect is defined as 3 meters seaward of the large tripod (LT). The distance between the large tripod (LT), the small tripod 1 (ST1) and the small tripod 2 (ST2) is 12 and 11 meters respectively (Figure 9). The distance between ST 2 and the small tripod 3 (ST3) is 35 meters. One Ossi's is located between ST2 and ST3 and the 4 other Ossi's are located landwards of ST3, with 2 Ossi's located at the seaward side of the beachplain and 2 Ossi's located at the landward side of the beachplain.

The top of the beachplain was located at approximately +1.5 meter above MSL. The locations of the ST's was located at respectively -0.65, -0.25 and 0.50 meter above MSL. The location of the LT was located at the seaward end of the transect at -0.90 meter above MSL.

The location of the measurement transect was placed accordingly to decrease the influence of the Slufter channel on the measurement locations and to increase the chance on complete measurement transect inundations during more severe weather conditions. For expected storm events, ST1 was transferred from its more seaward location to the top of the beachplain at  $x=166$  m from the seaward boundary. When ST1 was located on top of the beachplain, it is called ST1-storm.

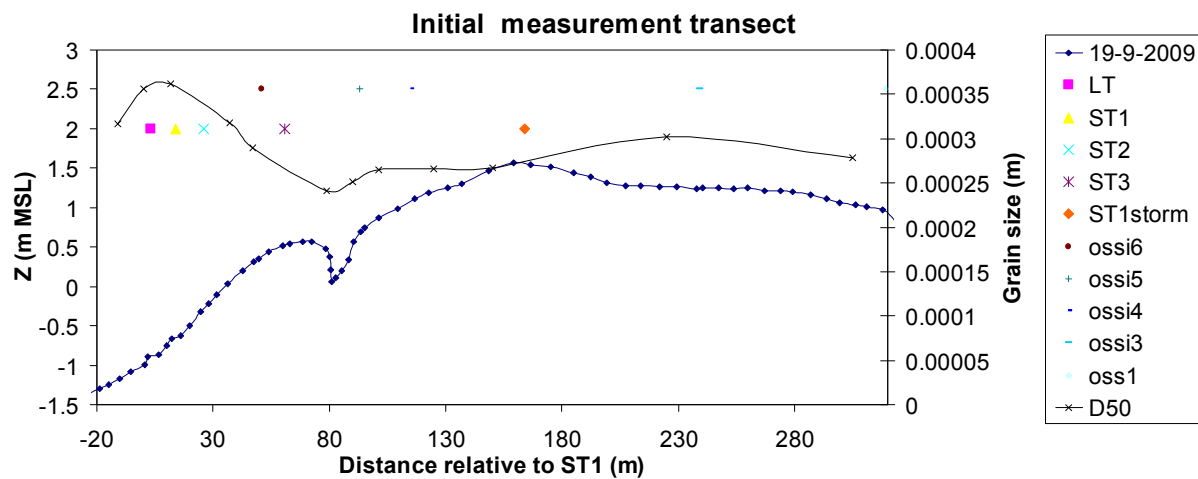


**Figure 9: Location of measurement instruments and median grain size along beach profile on September 19, 2009.**

In figure 9, the median grain size along the measurement transect is also depicted. The general trend is that the median grain size decreases towards higher elevated areas. Further offshore median grain size is between 300 and 350  $\mu\text{m}$ , whereas on the beachplain it lies between 250 and 300  $\mu\text{m}$ . The samples were taken in mid October (October 13-16). The median grain size was determined from the fall velocity. The fall velocity of the sediment samples was measured in a large water column in the lab.

During the field campaign, the height of each OSSI's above the bed was measured daily and if necessary the height of the sensor was adjusted and the information was logged. Via linear interpolation, the height of the sensor in time was estimated. The same is done for the measurement devices at all tripods, where the height of the measurement devices on the ST's is set back daily to its original position.

Table 1 shows the average heights of the measurement devices for the entire fieldwork. On September 26, the height of the EMF's above the bed was increased for ST1 and ST2 by 4 cm and by 2 cm for ST3 to mitigate the influence of swash on miniframe inundation. Observations showed that during swash, the miniframe sank approximately 4-5

centimeters in the sand. When the height of the OSSI sensor above the bed is larger than 30 cm, the height of the OSSI above the bed is set back to approximately 10 cm above the bed. Daily, the ST's were inspected, cleaned and set back to their original location and orientation. The height of the EMF above the bed was measured to determine the rate of sink and the height of the ST was set back to its original height of 22 or 24 cm above the bed. Since the first week the rate of sink was significant (especially during swash conditions), the initial height of the EMF above the bed was set to 25 and 24 cm for ST1 and ST2 respectively on September 26. The initial height of ST3 was kept constant at 22 cm above the bed due to a smaller rate of sink related to its more landward location. Data of the ST's was extracted daily with mini-laptops. Before data extraction, the clock of the laptops were synchronized and after data-extraction the time in the data logger of each tripod was set to the time of the laptops, resulting in that all tripods had a synchronized clock. Also, the LT was inspected and cleaned daily and the heights of the measurement devices above the bed were measured manually.

Location	hab EMF 1 (cm)	adjusted hab EMF 1 (cm)	hab EMF 2 (cm)	hab pressure sensor (cm)
LT	20-45		45-70	0-31
ST1	20	24		9
ST2	20	24		14
ST3	20	22		10
OSSI1				0-40
OSSI2				0-40
OSSI3				0-35
OSSI4				0-15
OSSI5				0-45

**Table 1: Height above the bed (hab in cm) of all measurement devices at each measurement location.**

Three times during the fieldwork, an extensive DEM was made using DGPS and topographical levelling data to monitor the larger scale morphodynamic development of the Slufter. The beach section of the Slufter is monitored by DGPS daily. The first DEM originates from the start of the fieldwork (Julian day 259), the second from after a major storm event on October 4 (Julian day 276) and the third at the end of the fieldwork (Julian day 304). The morphological evolution of the measurement transect is monitored by DGPS daily. Due to technical difficulties, no DGPS measurements were obtained between September 30 and October 6. Hence, no extensive DEM is available of the conditions before the major storm event of October 4.

Figure 10a shows a digital elevation model of the Slufter inlet at the onset of the campaign (September 20), whereas figure 10c shows a digital elevation model of the Slufter inlet at the end of the field campaign (October 30). The southern dune row is shown at the right of each image. Differences in height of the southern dune row between both figures are related to differences in measurement locations. The elevated area at the northeast side of the DEM's is a man-made obstruction to detain the Slufter channel from following its original course along the northern dune row. The man-made obstruction is attached to the northern dune row. Furthermore, the old Slufter channel is still present along the northern dune row. The most recent re-channeling of the Slufter channel occurred during spring 2009.

The beach of the Slufter inlet consist of a large intertidal area, with alongshore-variable intertidal bars and troughs and a supratidal beachplain around +1.5 m above mean sea level. As said, the hinterland is flooded diurnally via the Slufter channel and is in open contact with the North Sea. The Slufter inlet can be divided in two sections: one section north of the Slufter channel and one south of the Slufter channel. During the field campaign, ridge-runnel systems were present on the intertidal area with landwards migrating sand bars at both sections. The northern section showed much more alongshore variability than the southern section. The runnels in the southern section discharge into the Slufter channel, whereas the runnels in the northern section discharge via rip-currents to sea. The measurement transect was location on the southern beachplain.

At the mouth of the Slufter channel a sub-tidal delta is present, which built out southwards during the field campaign. This is seen by the infilling of the relative deep area seaward of the measurement transect.

Further offshore, subtidal sand bars are located, on which waves break already under moderate wave conditions and which are also seen partly in Figure 10. The subtidal bars are dissected by rip-currents.

The strongest impact of the storm on the area of the Slufter inlet is a decrease in alongshore-variable intertidal bars and troughs resulting in a more uniform beach (Figure 10b). Four days after the storm event, 3D patterns were scarcer than prior to the storm event. Furthermore, the outflow of the Slufter channel was directed more in westwards direction relative to moderate wave conditions, where the outflow is more southward directed (Figure 10a&b). This change in outflow direction is related to the strong increase in discharge after the storm event, causing the Slufter channel flow to straighten. A week after the storm, the Slufter channel discharged in a more southern direction again.

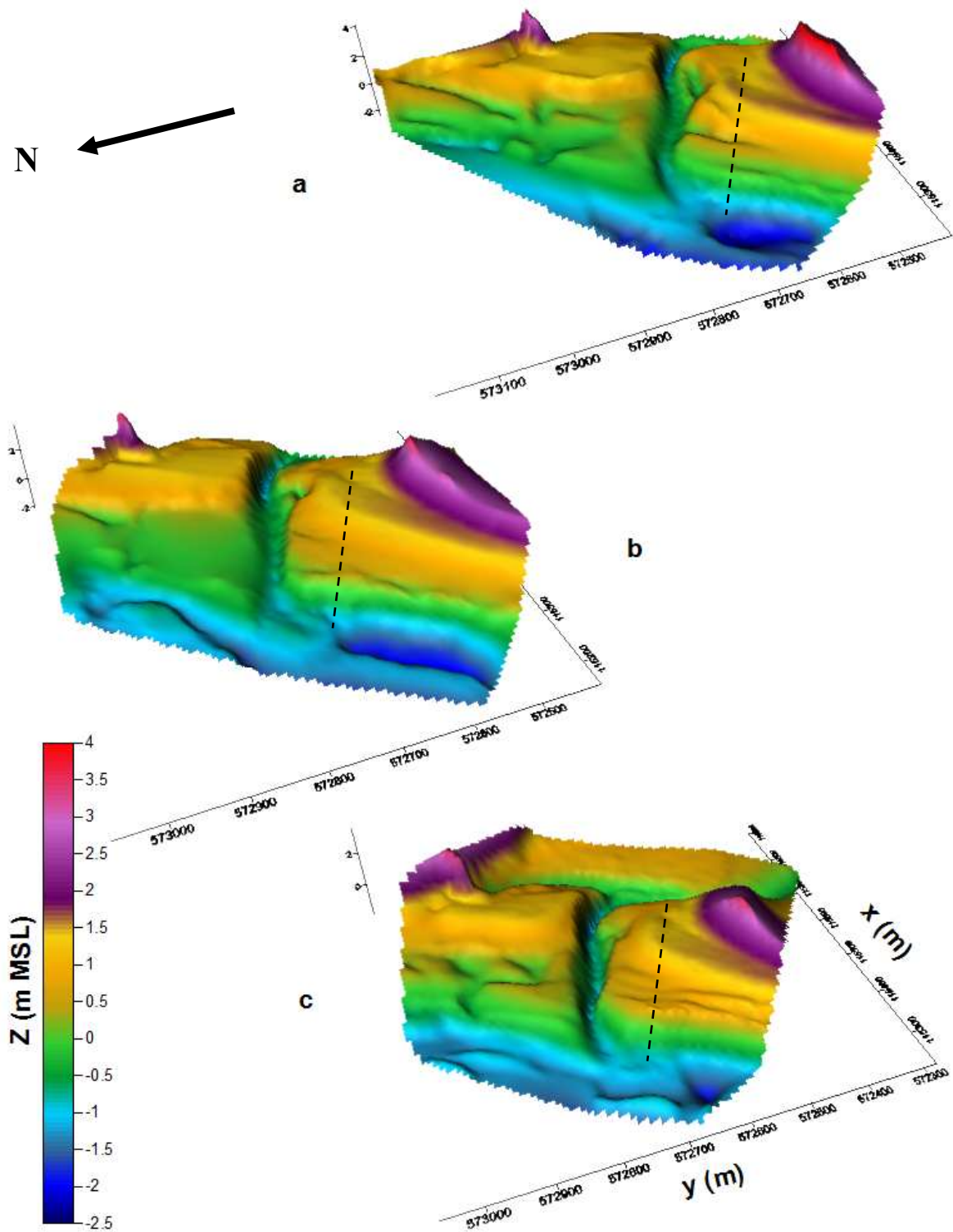


Figure 10: Digital Elevation Models of the Slufter inlet area: a) At start of measurement campaign (September 20), b) 4 days after the major storm event (October 8) and c) at the end of the field campaign (October 30).

Figure 11a shows the development of the measurement transect for every 2<sup>nd</sup> week. It shows that on September 18, two ridge runnel systems were present in the intertidal zone and that both runnels became shallower over the next 2 weeks and moved landwards. Onshore sand bar migration is also supported by the data from the activity rods. The storm-event resulted in a disappearance of the ridge-runnel systems and a decrease in elevation at the top and seaward side of the beachplain and an increase in elevation landwards of the top of the beachplain. After the storm event, new ridge/runnel systems developed of which the ridge moved landwards gradually as can be seen from October 21 and November 1. The landward side of the beachplain bordering the Slufter channel eroded significantly during the storm event due to increased outflow velocities.

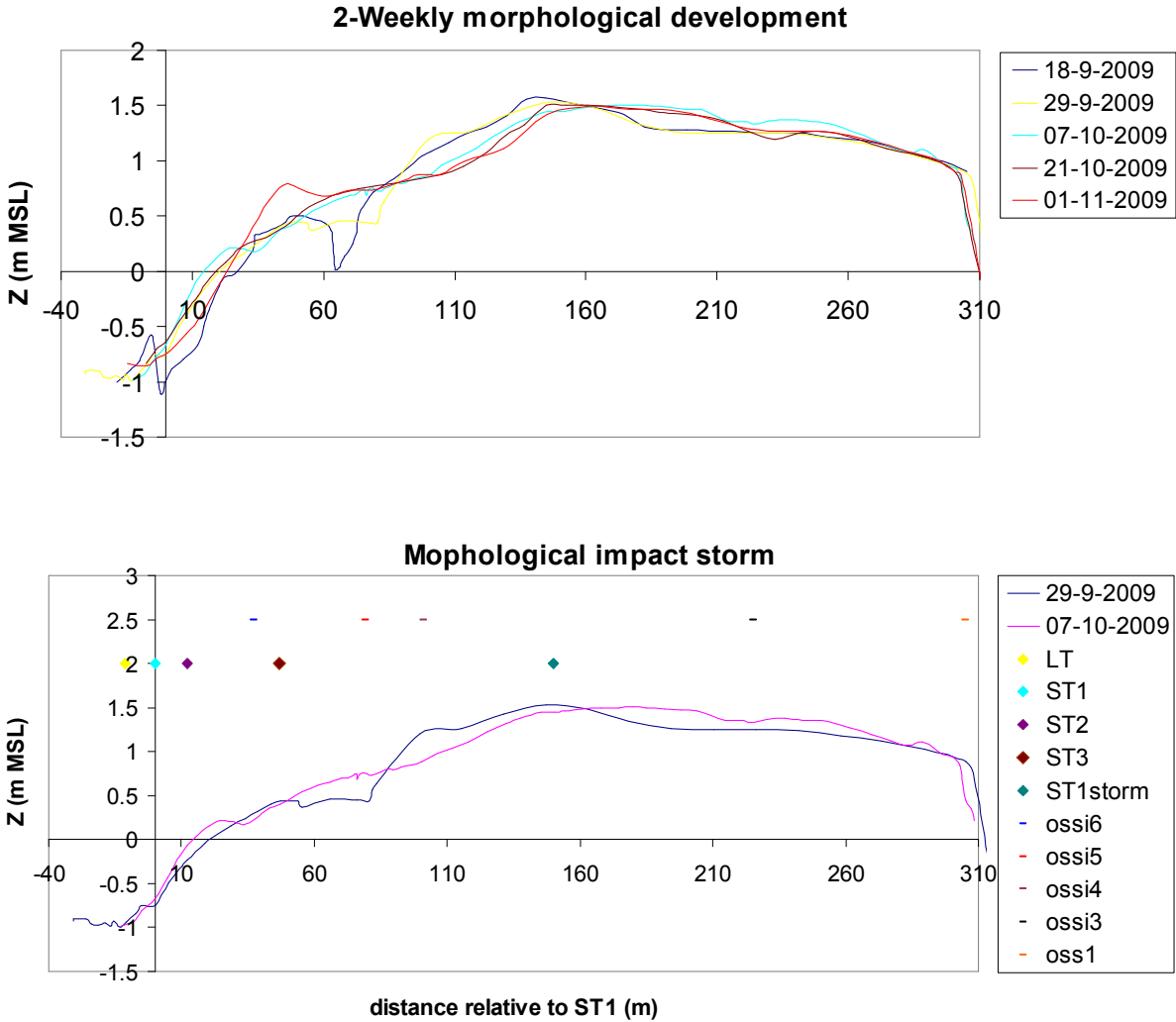


Figure 11: a) 2-weekly morphological development of measurement transect, b) Impact storm on morphological development of the measurement transect.

## 2.4 Data processing

After calibration of the dataset, several parameters were computed. Water depth is computed from the pressure data, by subtracting the air pressure and adding the instrument height.

For the entire dataset, the significant wave height ( $Hm0$ ) was computed for high- and low frequency ranges from the sea surface elevation data. First the sea surface elevation data was detrended with a second order polygon and then  $Hm0$  was computed for each 20 minutes with equation 3

$$Hm0_{fr} = 4 \sqrt{\frac{1}{N} \sum_{i=1}^N (SSE_{fr} - \overline{SSE_{fr}})^2}, \quad (3)$$

where  $Hm0$  is 4 times the standard deviation of the sea surface elevation for a defined frequency range ( $SSE_{fr}$ ). The low-frequency range is defined between 0.005 and 0.05 Hz and the high-frequency range lies between 0.05 and 1 Hz. The  $Hm0$  was computed at each tripod measurement location, because here also flow data was available enabling an better comparison between different parameter.

The mean wave angle and wave spread is obtained from principal component analysis of a detrended cross-shore and alongshore high-frequency(0.05-1 Hz) velocity signal, where the mean angle is related to the orientation of the first eigenvector and the wave spread is related to the square root of the relative contribution of the second eigenvector.

Velocity skewness is computed by the equation given below (Butt & Russel, 1999)

$$S_{fr} = \frac{\langle u_{fr}^3 \rangle}{\langle u_{fr}^2 \rangle^{\frac{3}{2}}}, \quad (4)$$

where  $S_{fr}$  is the amount of skewness (-) for a defined frequency range,  $u_{fr}$  is the instantaneous velocity (m/s) of a defined frequency range and the angle brackets denote time averaging. Sea surface elevation skewness is computed by replacing  $u_{fr}$  by  $p_{fr}$  of the pressure or instantaneous sea surface fluctuations (in meters). Together with wave asymmetry, wave skewness describes the transformation of the wave shape while the wave propagates onshore.

Asymmetry is computed with equation 5 (Elgar & Guza in Foster et al., 1999)

$$A_{fr} = \frac{\langle H(u_{fr})^3(t) \rangle}{\langle H(u_{fr})^2(t) \rangle^{\frac{3}{2}}}, \quad (5)$$

where  $A_{fr}$  is the amount of asymmetry (-) for a defined frequency range and where  $H(u_{fr})$  is the Hilbert transform of  $u_{fr}$  (m/s) of a defined frequency range. Sea surface elevation asymmetry is computed by replacing  $u_{fr}$  by  $p_{fr}$ , where  $p$  is the instantaneous sea surface elevation in meters. Skewness and asymmetry is computed for the high- and low- frequency domain.

Comparison between low- and high-energetic conditions is done for a 90 minutes time series, which is the shortest time period the water level is stationary at the most landward tripod measurement location. Low-energetic, or moderate weather, conditions are defined as having a  $Hm0_{offshore}$  smaller than 2 m and high-energetic, or storm weather, conditions are defined as having a  $Hm0_{offshore}$  larger than 4 m. All parameters described above are also computed for the low- and high-energetic scenarios. Plus the cross-shore and alongshore root mean square velocity ( $u_{rms}$  and  $v_{rms}$ ) are computed from the variance of the cross- and alongshore velocity signal ( $u$  and  $v$ ).

$$u_{rms} = \sqrt{\text{var}(u)}, \quad (6)$$

$$v_{rms} = \sqrt{\text{var}(v)}, \quad (7)$$

Also, the spectral densities (PP) of the sea surface elevation data are computed at each measurement location. To increase the degrees of freedom for the spectral analysis, the block size is changed from 20 to 15 minutes (3600 samples tripods, 4800 samples Ossi's) for the low- and high-energetic scenarios. For the spectral analysis, the degrees of freedom are to 28, the spectral resolution to 0.0011 Hz and the confidence interval increases to 0.6298 and 1.8291 for the lower and upper side respectively.

The phase difference in sea surface elevation between the LT and the more landward located measurement locations was computed with cross-spectral analysis ( $PP_{co}$ ) using blocks of 15 minutes with 50% overlap and using the Hamming window in order to investigate the cross-shore infragravity wave pattern.. Since the tripods measured with sample frequency of 4 Hz and the OSSIs with a sample frequency of 5 Hz, the OSSIs data is converted from a 5 Hz

time series to a 4 Hz time series by interpolation. At the end of every burst of each OSSI, 1 minute of data is lacking, which is filled with the mean water depth to make computation of the phase difference between the LT and the OSSI's possible. The phase difference is computed by taking the inverse tangent of the imaginary and real part of  $PP_{co}$ .

Also, the coherence between the LT and the more landward located measurement locations is investigated to determine the cross-shore infragravity wave pattern

$$C_{xy}(f) = \frac{|PP_{xy}(f)|^2}{PP_x(f)PP_y(f)}, \quad (8)$$

Where  $C_{xy}(f)$  is the coherence (-) between the spectral densities (PP) at x (LT) and y (other measurement location) at a certain frequency.  $PP_{xy}$  is the cross-spectral power spectral density of x and y.

Another method of investigating the cross-shore infragravity wave pattern is with energy fluxes. Infragravity wave energy fluxes were decomposed into a shoreward ( $F^+$ ) and seaward ( $F^-$ ) propagating component, assuming shore-normal wave propagation, following Sheremet et al. (2002)

$$F^\pm = \frac{\sqrt{gh}}{4} \int (PP + \frac{h}{g}UU \pm \sqrt{\frac{4h}{g}}PU)df, \quad (9)$$

where  $PP(f)$  and  $UU(f)$  are the auto-spectra of pressure and cross-shore velocity respectively,  $PU(f)$  is the cross-spectrum of pressure and cross-shore velocity, and the integral is over the infragravity frequency ( $f$ ).  $PU(f)$  is a matrix of complex numbers. To compute  $F^\pm$ , the real part of  $PU(f)$  is used.

The reflection of infragravity waves is estimated by dividing the energy fluxes with each other

$$R^2 = \frac{F^-}{F^+}, \quad (10)$$

where  $R^2$  is the infragravity reflection coefficient, or the bulk infragravity reflection coefficient (-). A  $R^2$  of 1 at the shoreline indicates shoreline reflection of infragravity waves.

### 3. Entire field campaign

In this section the nearshore wave characteristics of low and high-frequency waves during the entire field campaign at each tripod measurement location is analyzed in order to establish the relative contribution of low- and high-frequency wave at the Slufter.

#### 3.1 Wave characteristics

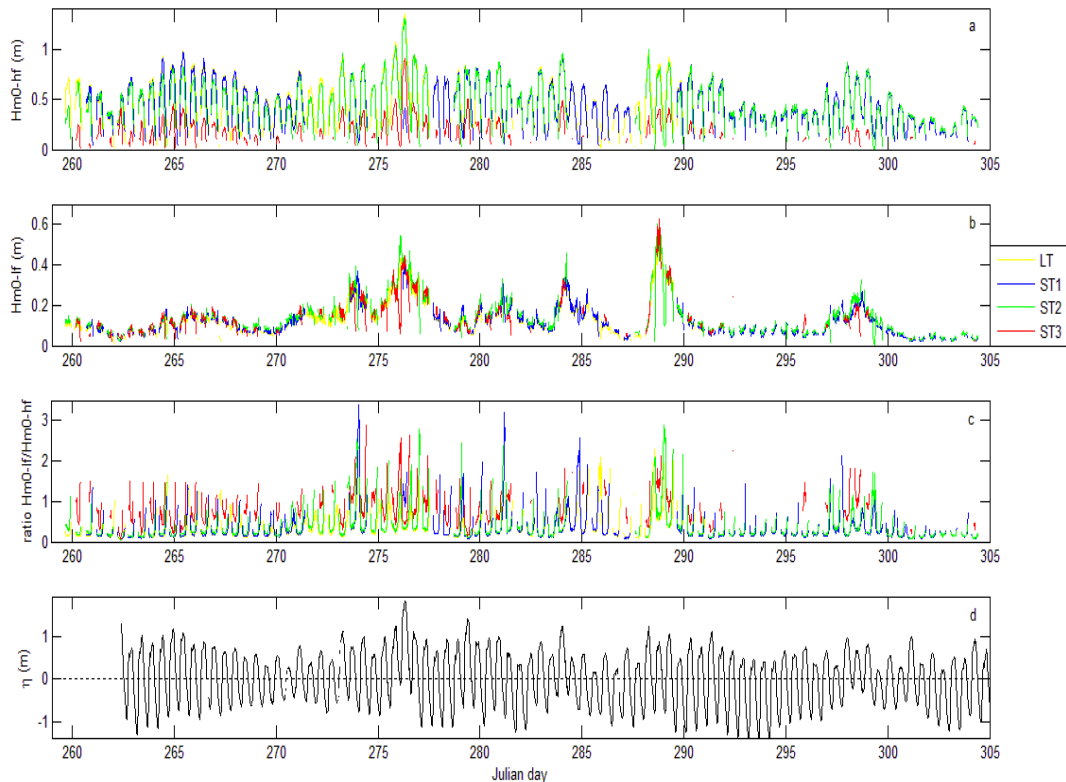


**Figure 12: Significant wave height ( $H_{m0}$ ) for each tripod measurement location: a)  $H_{m0}$  (hf) (f [0.05-1]), b)  $H_{m0}$  (lf) (f[0.005-0.05]), c) ratio between  $H_{m0}$  (lf)/ $H_{m0}$  (hf), d) Offshore water level fluctuations.**

Figure 12 shows the significant wave height during the measurement campaign for different frequency ranges. Between Julian day 274 and 277, ST 1 was located on top of the beachplain (ST1-storm). A strong increase in high-frequency significant wave height,  $H_{m0}$  (hf), in the nearshore occurred during the storm event on October 4, on Julian day 276 and a smaller increase occurred during the storm event on October 16, on Julian day 288, the difference in increase is related to a difference in storm surge magnitude (Figure 12d).  $H_{m0}$  (lf) increased with approximately the same magnitude during both storm events.

An increase in Hm0 Offshore results in an increase in Hm0 (lf) (Figure X13) as also witnessed by Masselink (1995), Raubenheimer et al. (1996) and Ruessink (1998a). Hm0 (lf) increases with 0.081-0.089 m per m Hm0 Offshore increase and increases most strongly at the middle, ST2, tripod measurement location.

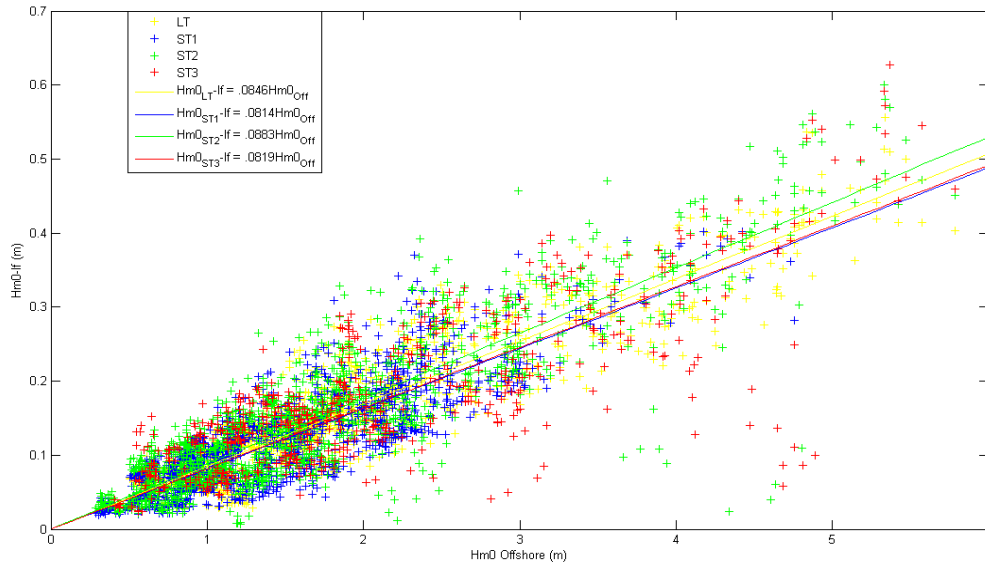


**Figure 13: Correlation between Hm0 Offshore (m) and Hm0 (lf) (m) per tripod location.**

In figure 14 the Hm0 (hf&lf) and its ratio is depicted during several tidal cycles. Hm0 (hf) decreases towards the shore, whereas Hm0 (lf) remains the same or even increases slightly depending on offshore wave conditions as is, indicating shoaling of low-frequency waves. This corresponds with observations from Guza & Thornton (1985), Ruessink (1998a), Aagaard & Bryan (2003) and Karunarathna & Chadwick (2007).

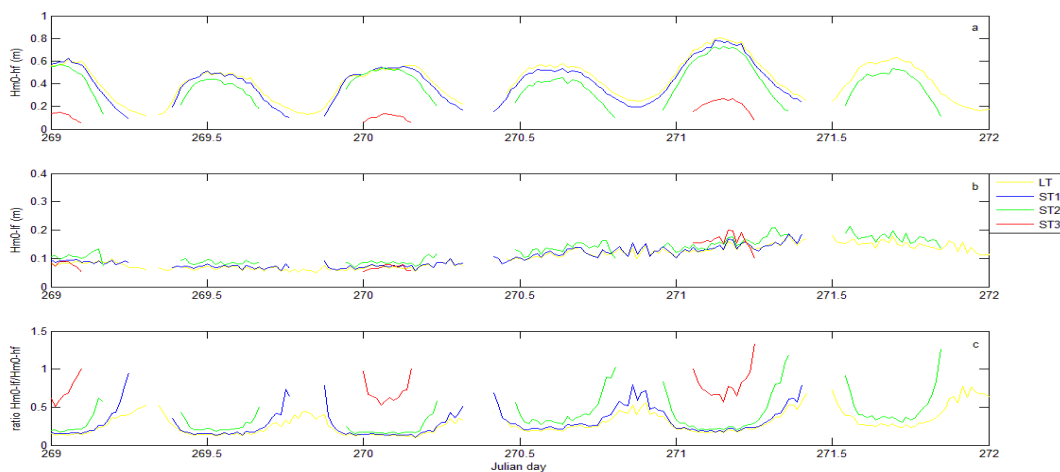


**Figure 14: Hm0 at each measurement location between Julian day 269 and 272. a) Hm0 (hf), b) Hm0 (lf), c) ratio between Hm0 (lf) and Hm0 (hf).**

The fluctuating pattern of  $Hm0$  ( $hf$ ) with the tide indicates wave breaking. A good way to know in which hydrodynamic conditions (shoaling, surf, swash) and for what duration the measurement locations are located in each zone is by using the hydrodynamic zone and residence times concept described by the Masselink et al. (2006) and Price&Ruessink (2008).

Residence times are an indication of the time period the distinct hydrodynamic processes related to a specific hydrodynamic zone play a role at a certain. Generally, the boundary between the shoaling, surf and swash zone is determined by  $Hm0/h$ , where the boundary between the shoaling and surf zone varies between 0.3 and 0.7 and the boundary between the surf and swash zone varies between 0.7 and 1 (Masselink et al., 2006). However, Raubenheimer et al. (1996) and Price & Ruessink (2008) found that the boundaries between the hydrodynamic zones depend on wave length instead of on the ratio of  $Hm0/h$ , which signifies that the assumption of a spatially constant and time-independent relative wave height is not valid. The boundaries between the hydrodynamic zones can be determined by the equations given below

$$L = T_{m01} \sqrt{gh}, \quad (11)$$

$$\left[ \frac{Hm0(hf)}{h} \right]_b = 6.1 \frac{Hm0(hf)}{L} + 0.31, \quad (12)$$

$$\left[ \frac{Hm0(hf)}{h} \right]_s = 29 \frac{Hm0(hf)}{L} + 0.35, \quad (13)$$

where the wave length is computed with equation 11 with  $T_{m01}$  being the reciprocal of the centroidal frequency (s),  $g$  being the gravitational acceleration ( $9.81 \text{ m/s}^2$ ) and  $h$  being the water depth (m).  $T_{m01}$  is determined from the maximum spectral density of the high-frequency range. Spectral analysis was done for a 20 minute time period (4800 samples) with a block size of 6.66 minutes (1600 samples) using a Hamming window. The lower and upper limits of the confidence interval were 0.53 and 2.6 respectively. The number of degrees of freedom were 13 and the spectral resolution was 0.0022 Hz.

Equation 12 computes the boundary between the shoaling and surf zone where subscript  $b$  indicates the boundary between the shoaling and surf zone, which was determined to vary between 0.3 and 0.85 and which depended linearly on the local wave steepness. Equation 13 computes the boundary between the surf and swash zone where the boundary

between the surf and swash zone lies between 0.5 and 1.9. The mean hydrodynamic boundaries of the entire data set for the shoaling/surf zone and the surf/swash zone are 0.43 and 0.95 respectively.

Table 2 shows the residence time for the tripods during the entire field campaign. As expected, the residence time of the shoaling zone decreases onshore across the measurement transect, whereas the residence time of the swash zone increases onshore. The entire measurement transect except for ST2 resides about 55% of the inundated time in the surf zone, whereas ST2 is exposed 75% of the time to surf zone conditions. It must be mentioned that difference between spring- and neap tide are not taken into consideration.

	shoaling	surf	swash	totLoc
LT	41	54	5	1
ST1	34	55	11	1
ST2	14	77	9	1
ST3	3	55	42	1
totZone	21	60.25	16.75	-

**Table 2: Residence times (in %).**

Residence times and the location of the hydrodynamic zones also differ per tidal cycle. Mean water depth differs up to 0.5 meter between sequential cycles, resulting in a change in the location of the hydrodynamic zones. Also, differences in water depth related to the spring/neap tide cycle are an important factor influencing the location of the hydrodynamic zones and its residence times. Offshore conditions also play an important role (Figure 13).

Furthermore, the location of the hydrodynamic zones changes over a tidal cycle. During the rising and falling of the tide, hydrodynamic conditions change over distance and the ratio between  $H_{m0}(lf)$  and  $H_{m0}(hf)$  changes strongly, which is shown by the approximate parabolic shapes of the ratio per tidal cycle (Figure 14). During high water, the ratio is constant, since the hydrodynamic conditions do not change strongly due to tidal water depth fluctuations. During neap tide, the ratio is expected to be larger due to a more offshore located surf zone, resulting in a breaking of high-frequency waves at a more offshore location. However, no trend is found (Figure 12) and a stronger correlation is found between the ratio and offshore wave height (Figure 13). An increase in offshore  $H_{m0}(hf)$  results in a broadening and a seaward shift of the outer edge of the surf zone and in an increase in the ratio between  $H_{m0}(lf)$  and  $H_{m0}(hf)$  at a measurement location.

The ratio between  $H_{m0}(lf)$  and  $H_{m0}(hf)$  in figures 12c and 14c shows that an increase in dominance of low-frequency waves over high-frequency waves occurs towards the shore. In figure 15 the relation between the magnitude of the  $H_{m0}(lf)$  and the magnitude of the  $H_{m0}(hf)$  for each hydrodynamic zone is depicted. Even though the spread is large, there is a trend that the ratio between  $H_{m0}(lf)$  and  $H_{m0}(hf)$  increases from the shoaling zone towards the swash zone. Table 3 shows that the mean ratio between  $H_{m0}(lf)$  and  $H_{m0}(hf)$  more than doubles from the shoaling zone (0.21) towards the swash zone (0.52). The variance quadruples (0.06 to 0.24). So, the dominance of low-frequency waves over high-frequency waves more than doubles from the shoaling towards the swash zone, but the variance increases even more. The magnitude of  $H_{m0}(hf)$  does remain larger than the magnitude of  $H_{m0}(lf)$ .

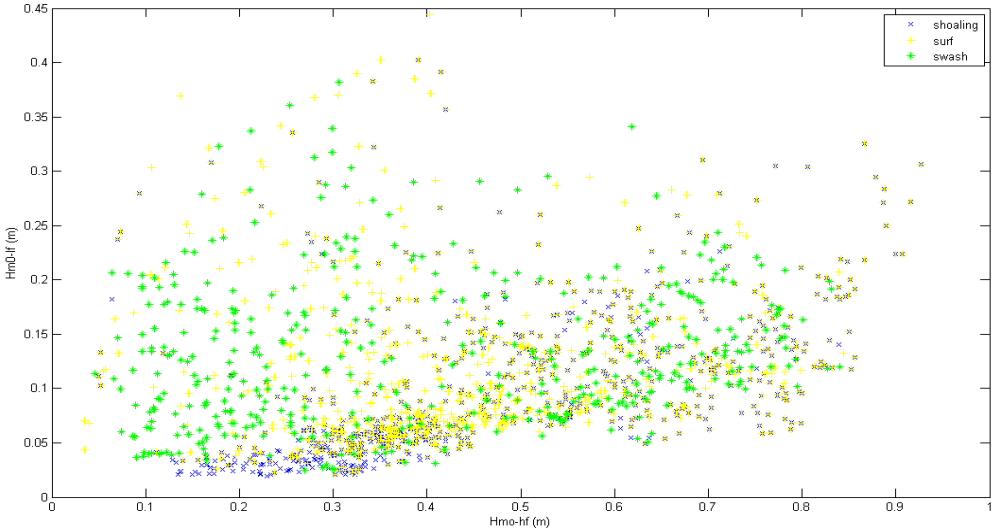


**Figure 15: Ratio between  $H_{m0}(hf)$  and  $H_{m0}(lf)$  for the different hydrodynamic zones.**

ratio $H_{m0}(lf)/H_{m0}(hf)$	shoaling	surf	swash
mean	0.21	0.29	0.52
variance	0.06	0.08	0.24

**Table 3: mean and variance of the ratio  $H_{m0}(lf)/H_{m0}(hf)$  for each hydrodynamic zone.**

Figure 16 shows the wave angle and wave spread of the tripods during the entire field campaign. It shows that the wave angle decreases onshore, which is expected when refraction is the nearshore is considered. It also indicates that the orientation of the measurement locations is not exactly in cross-shore direction, since the wave angle with the shore-normal becomes negative, indicating that the tripods are not always oriented exactly shore-normal.

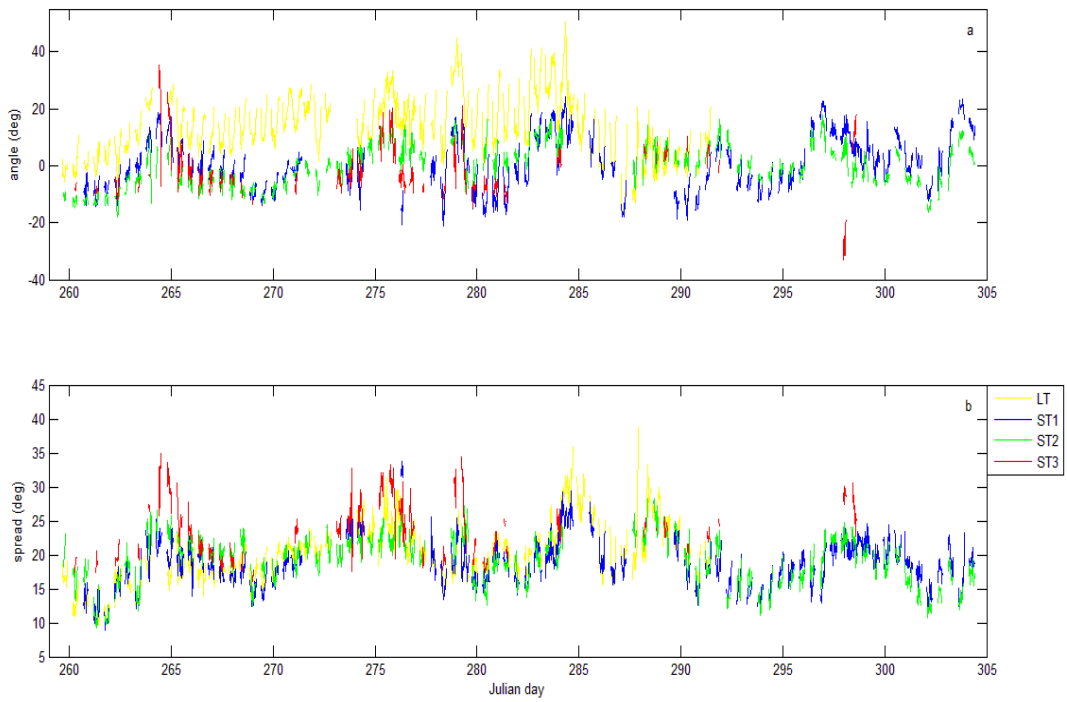


**Figure 16: a) Wave angle and b) wave spread of all tripods locations during the field campaign.**

### 3.2 Skewness and asymmetry

In figures 17 the velocity skewness and asymmetry for high- and low-frequency waves against  $Hm_0/h$  is depicted. High-frequency skewness is already positive from  $Hm_0/h$  is 0.15, indicating shoaling of high-frequency waves (Figure 17a). Due to shoaling, the wave crest becomes more sharply peaked and the wave trough becomes more flat and broad until  $Hm_0/h$  is 0.35-0.4 and with skewness values around 0.6. For increasing  $Hm_0/h$ , wave breaking occurs and the wave shape becomes less skewed and skewness decreases again to values around 0.4. The mean boundary between the shoaling and surf zone is smaller than the mean value of 0.44 found with the method of Price&Ruessink (2008), where also the wave length is taken into consideration.

Low-frequency velocity skewness waves fluctuates around zero for the entire  $Hm_0/h$  range except for deeper water conditions between  $Hm_0/h$  0.2-0.3, where the velocity skewness is negative up to -0.2, indicating that the wave crests slightly flatten and become more broad and that the wave trough becomes slightly sharply peaked (Figure 17b). It suggests that low-frequency waves may already transform slightly for small  $Hm_0/h$  values.

In figure 17c the high-frequency velocity asymmetry is depicted, which is already negative for small  $Hm_0/h$  values and becomes more negatively asymmetric for increasing  $Hm_0/h$  values. Waves become asymmetric just prior to wave breaking and continue to become more asymmetric after wave breaking. The negative asymmetry means that the wave become pitched forward with steep front faces and more gently sloping rear faces (Austin et al., 2009 and many others). The mean high-frequency velocity asymmetry at  $Hm_0/h$  is 0.75 is approximately -0.7. Low-frequency velocity asymmetry is small and remains approximately 0 for higher  $Hm_0/h$  values even though a small increasing negative asymmetry trend is distinguishable.

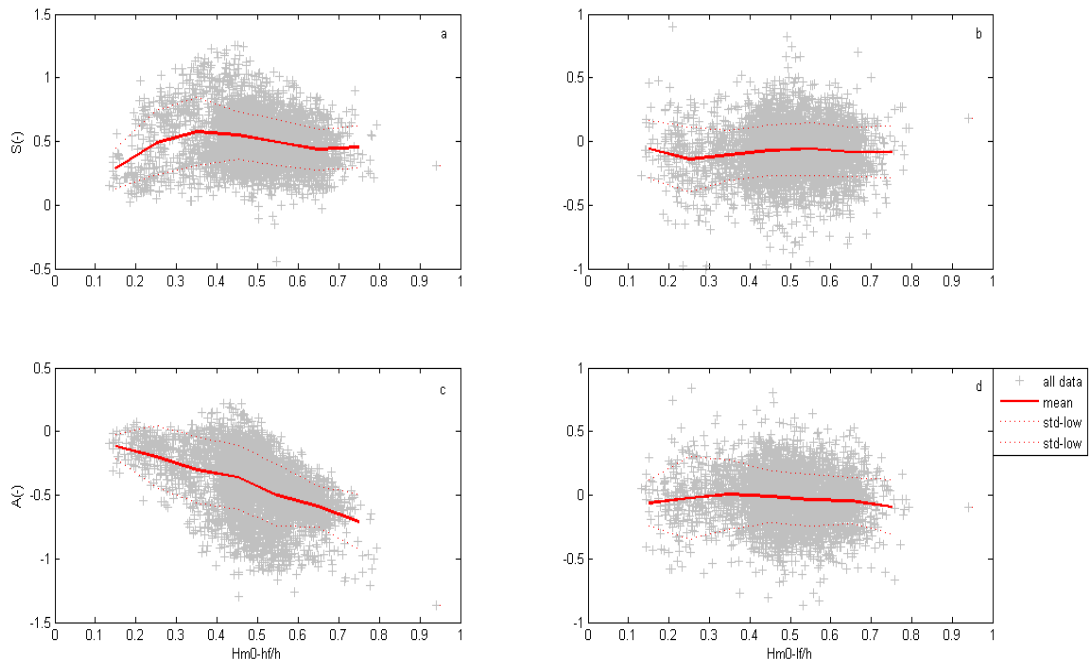


**Figure 17: Skewness and asymmetry of all measurement locations against  $H_{m0}/h$ : a) velocity skewness of high-frequency range, b) velocity skewness of low-frequency range, c) velocity asymmetry of high-frequency range, d) velocity asymmetry of low-frequency range.**

Figure 18 shows the skewness and asymmetry as described above, but per measurement location and in time. The measurement locations experiencing the most surf zone conditions, ST1 and ST2, show the highest high-frequency skewness values, whereas the measurement devices located landward and most in the swash zone (ST3) have smaller high-frequency skewness values (Figure 18a). It indicates that the boundary between the shoaling and surf zone is mostly frequently located between ST1 and ST2, which corresponds with the residence time computations (table 2). Low-frequency skewness is of a similar magnitude during the field campaign and no trend in the cross-shore direction is present (Figure 18b).

Figure 18c shows that high-frequency waves become more negatively asymmetric towards the shore. Low-frequency velocity asymmetry remains constant during the field campaign.

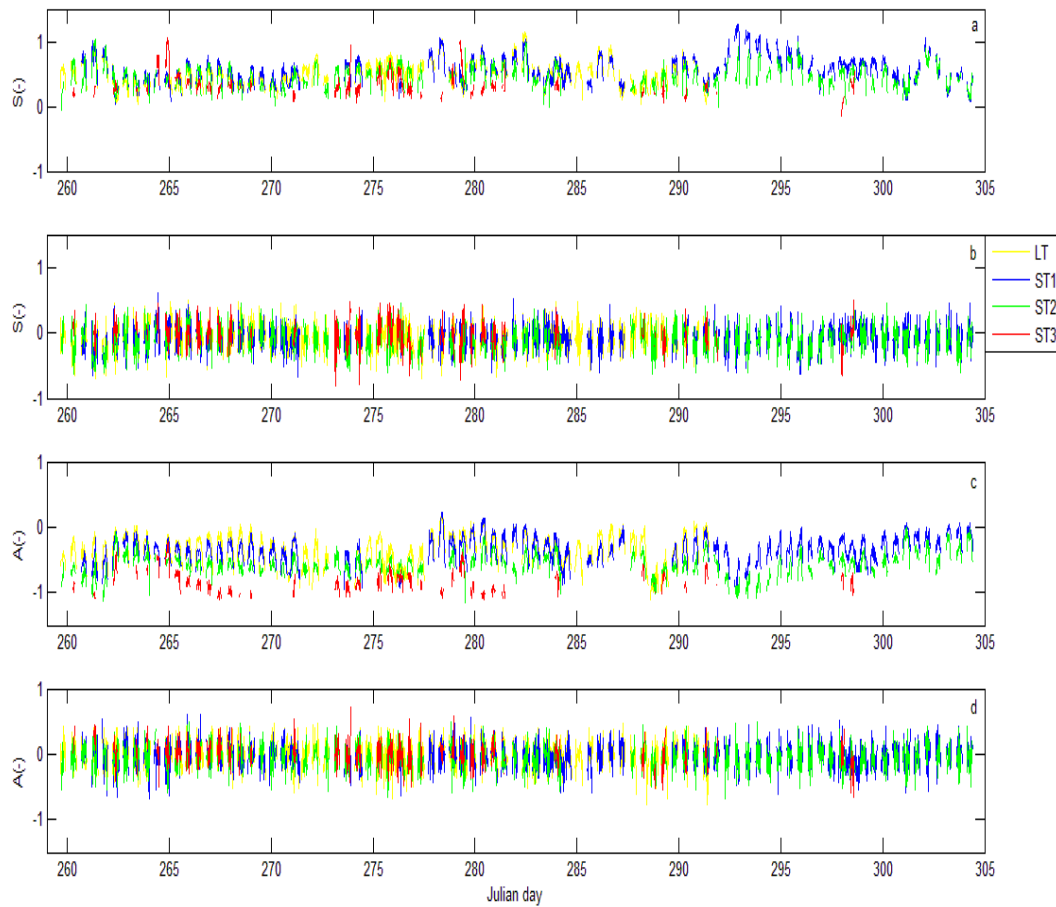


**Figure 18: Skewness and asymmetry of all measurement locations against time: a) velocity skewness of high-frequency range, b) velocity skewness of low-frequency range, c) velocity asymmetry of high-frequency range, d) velocity asymmetry of low-frequency range.**

### 3.3 Conclusion nearshore wave characteristics

During the field campaign,  $H_{m0}$  (hf) decreases towards the shoreline, whereas  $H_{m0}$  (lf) remains constant in the surf zone and sometimes even increases slightly, which is also observed by Guza & Thornton (1985), Ruessink (1998a), Aagaard & Bryan (2003) and Karunaratna & Chadwick (2007).  $H_{m0}$  (lf) becomes larger with increasing  $H_{m0}$  Offshore.  $H_{m0}$  (lf) in the nearshore increases by 0.08 m per 1 m  $H_{m0}$  Offshore increase. The increase in  $H_{m0}$  (lf) with an increase in  $H_{m0}$  Offshore corresponds with findings from Masselink (1995), Raubenheimer et al. (1996) and Ruessink (1998a).

During a tidal cycle, the ratio between  $H_{m0}$  (lf) and  $H_{m0}$  (hf) is largest during the rise and fall of the tide and is also largest closer to the shoreline. Dominance of  $H_{m0}$  (lf) over

$H_{m0}$  (hf) increases by a factor 2.5 from the shoaling towards the swash zone from 0.21-0.52. However, the variance also increases by a factor 4 from 0.06 to 0.24.

High-frequency wave skewness reaches a maximum of around 0.44 between 0.35-0.40  $H_{m0}$ , which is a slightly smaller  $H_{m0}$  value for the seaward surf zone boundary as determined with the method of Price&Ruessink (2008), which includes wave length. After skewness has reached its maximum, it decreases again to values around 0.4. Low-frequency wave skewness is negative and of a smaller magnitude than high-frequency skewness. The minimum low-frequency skewness is already reached at 0.28  $H_{m0}/h$  with a value of -0.2 after which skewness goes back to 0 again. It suggests that low-frequency wave transformation.

High-frequency wave asymmetry becomes increasingly negative for increasing  $H_{m0}/h$  values, whereas low-frequency wave asymmetry fluctuates around zero for the entire  $H_{m0}/h$  range.

The shape of high-frequency waves becomes increasingly non-linear towards the shore, with increasing positive skewness towards the seaward boundary of the surf zone after which it decreases again and with negative asymmetry increasing onshore. The shape of low-frequency waves becomes only slightly non-linear towards the shore with negative skewness already occurring for small  $H_{m0}/h$  value, after which it decreases again back to zero. Low-frequency waves do not become asymmetric for increasing  $H_{m0}/h$  values. Butt & Russel (1999) found that infragravity waves also become negatively skewed in the nearshore but only during high-energetic conditions and that the negative skewness increases onshore which contradicts with findings from this study. The exact processes resulting in this increase in negative skewness are unknown. In the next chapter a more thorough analysis of low-frequency wave behaviour at the Slufter under different energetic conditions is done.

## 4. Infragravity wave behaviour during low- and high-energetic conditions

In this chapter, a comparison between infragravity wave behaviour during low- and high-energetic conditions is performed. In section 4.1, characteristics of the analyzed tidal cycles are discussed. In section 4.2, the relative contribution of low- and high-frequency waves during low- and high-energetic conditions is investigated. In section 4.3, a spectral analysis on the analyzed tidal cycles is performed. In section 4.4, the cross-shore infragravity wave pattern is examined by analyzing the phase difference and coherence between measurement locations. In section 4.5, the cross-shore shore infragravity wave pattern and reflection is examined by investigating the low-frequency wave energy fluxes.

### 4.1 Characteristics of tidal cycles

In figure 19, the profile of the beachplain during the analyzed tidal cycles is depicted. In figure 19a and 19b, the profile of the beachplain on October 7, Julian day 279, and on September 29, on Julian day 276, respectively is depicted. Due to technical difficulties, no profile could be obtained one day prior to the occurrence of the storm event of October 4. The last profile available before the storm event was on September 29. The seaward boundary of the measurement transect ( $x=0$ ) is located at 3 meters seaward of LT.

The profile on October 7 is relatively uniform with only one bar present at  $x=40$  m. During the storm event all pre-existing 3D-patterns were wiped out from the beach face resulting in an almost uniform beach. The beach uniformity after the storm event of October 4 was also observed in the field. Due to the absence of 3D beach morphology, a tidal cycle on October 7 with low-energetic conditions is used to analyze infragravity wave behaviour during low-energetic conditions.

The profile of the beachplain during the high-energetic conditions of October 4 is only expected to be present during the start of the tidal cycle (Figure 19b). It is expected that the beach face will become uniform during the storm. Therefore, it is expected that the beach morphology is uniform for both analyzed tidal cycles. Seaward of the top of the beachplain, between  $x=3$  and  $x=160$  m, the slope of the measurement transect is 0.0155 for both profiles. At the landward side of the top of the beachplain, between  $x=166$  and  $x=310$  m, the slope is -0.0033.

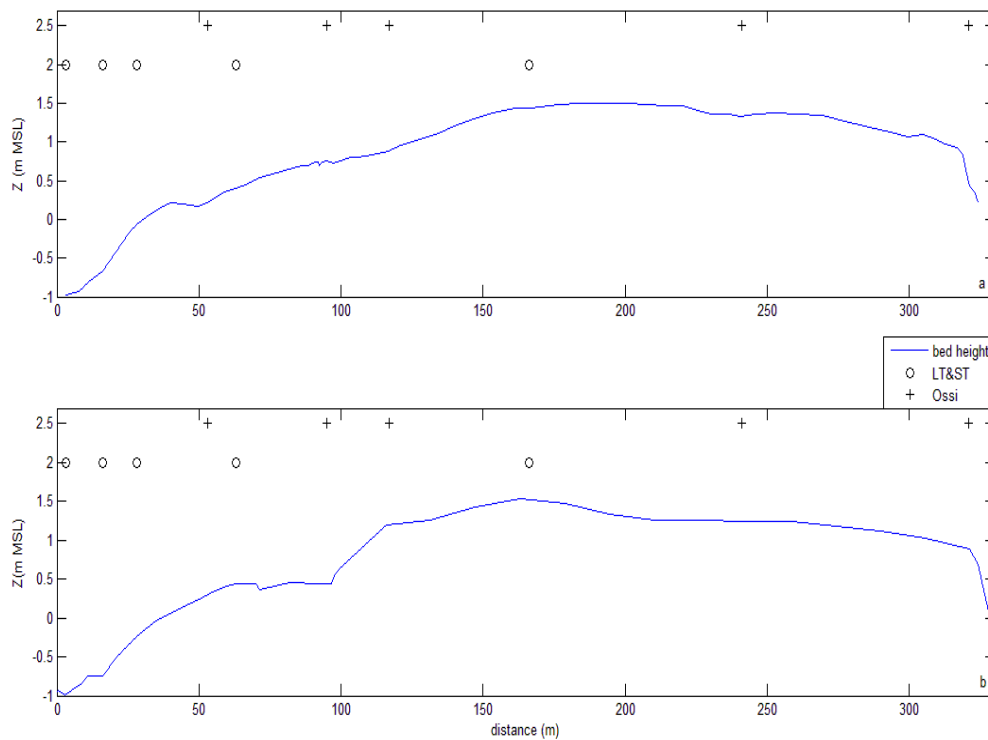


**Figure 19: Profile of the beachplain during low- and high-energetic conditions on October 7 (a) and before the high-energetic conditions of October 4 on September 29 (b) respectively.  $x=0$  is 3 m seaward of LT. Measurement locations are indicated with the open dots from the seaward to the landward side measurement locations are: LT, ST1, ST2, ST3 and ST1-storm. Pressure sensors are the cross-symbols, from the seaward side across the beachplain: OSSI 1, OSSI 2, OSSI 3, OSSI 4, OSSI 5.**

Figure 20 shows the 20 minute-averaged water depth fluctuations for the low- and high-energetic analyzed tidal cycles at each tripod measurement location. The two different energetic conditions have distinct trends concerning water level fluctuations and both trends become more pronounced towards the shore. During low and high-energetic conditions the rise of the tide occurs more quickly than the fall of the tide. During low-energetic conditions, after the first rise of the tide, the water level falls again slightly after which it rises again to a second slightly higher peak. During high-energetic conditions, the rise of the tide is followed by a stationary part after which the tide increases again by 0.5 m, reaching its peak and becoming stationary before falling again.

During the stationary part of the peak of the flood during low-energetic conditions, the mean water depth is 1.5 m at the seaward side of the measurement transect decreasing to 0.5 m at the landward side of the measurement transect. During the stationary part of the peak of the flood during high-energetic conditions, the mean water depth is 3 m at the seaward side of

the measurement transect decreasing to a mean water depth of 0.85 meter on top of the beachplain at measurement location ST1-storm.

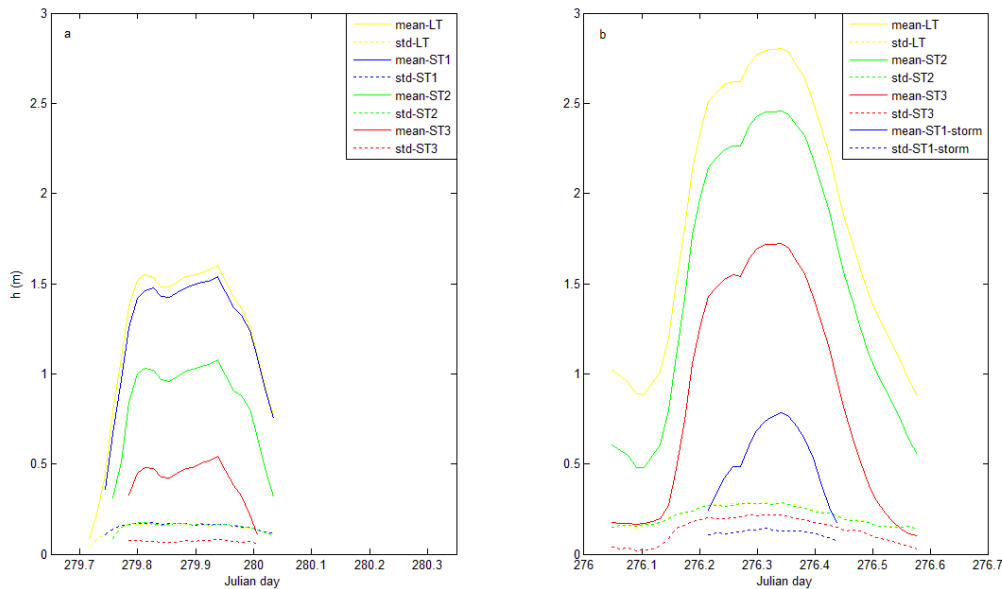


**Figure 20: 20 minute-averaged water depth and standard deviation of analyzed tidal cycles for (a) low-energetic conditions and (b) high-energetic conditions.**

Computational results on infragravity waves are only reliable when the water level is stationary for a time period larger than one hour. Therefore, analysis of infragravity wave behaviour can only be done during the peak of the flood. A discrimination between ebb and flood can not be made as is done by Thomson et al. (2006). The shortest stationary section is located at the most landward side of the measurement transect. A stationary time period of maximum 90 minutes is possible on top of the beachplain during high-energetic conditions. The time periods chosen are October 7 from 21:10:00 until 22:40:00 and October 4 from 07:20:00 until 08:50:00 for low-energetic and high-energetic respectively. In Julian days, both time period are 279.8819 to 279.9444 and 276.3056 to 276.3681 for low-energetic and high-energetic conditions respectively.

In table 5,  $H_{m0}$  ( $h_f$ ) and the boundaries of each hydrodynamic zone at each measurement location is given. During low-energetic conditions, offshore wave height is up to 1.5 m.  $H_{m0}$  ( $h_f$ ) at the seaward side of the measurement transect is 0.77 m until ST2, which is the boundary of the shoaling zone.  $H_{m0}$  ( $h_f$ ) decreases to 0.27 m in the surf and swash zone (Ossi 1 until Ossi 3).

During high-energetic conditions, offshore wave height was up to 5 m and  $H_m0$  (hf) was 1.29 m at the seaward side of the measurement transect. The surf zone was wider and the shoaling zone was located more seaward. On top of the beachplain, a  $H_m0$  (hf) of 0.40 m was measured. The boundaries of the hydrodynamic zones as a function of the relative wave height decrease onshore. This corresponds with Raubenheimer et al. (1996) who already discussed that the assumption of spatially constant and time-independent hydrodynamic boundaries is not correct.

	$H_m0$ (hf) low-E	Hyd zone	Bnd sh/su	Bnd su/sw		$H_m0$ (hf) high-E	Hyd zone	Bnd sh/su	Bnd su/sw
Offsshore	1.5	..	..	..	Offsshore	5	..	..	..
LT	0.79	shoaling	0.54	1.43	LT	1.36	shoaling	0.46	1.06
ST1	0.79	shoaling	0.58	1.64	ST2	1.34	surf	0.41	0.82
ST2	0.78	surf	0.59	1.70	Ossi1	1.14	surf	0.48	1.17
Ossi1	0.39	surf	0.48	1.17	ST3	0.98	surf	0.36	0.58
ST3	0.32	surf	0.38	0.69	Ossi2	0.81	surf	0.41	0.81
Ossi2	0.20	swash	0.41	0.81	Ossi3	0.75	surf	0.37	0.66
Ossi3	0.13	swash	0.37	0.66	ST1-storm	0.57	surf	0.49	1.18
					Ossi4	0.55	surf	0.35	0.56
					Ossi5	0.46	shoaling	0.34	0.49

**Table 4:  $H_m0$  (hf) at each measurement location and the relative wave height of the hydrodynamic boundaries of each measurement location during low- and high-energetic conditions ( $H_m0$  (hf)/h values for boundary shoaling and surf zone,  $H_m0$  (hf)/h values for boundary surf and swash zone).**

In figure 21, the cross-shore (u) and alongshore (v) velocities of each measurement location for low- and high-energetic conditions are depicted. For both energetic conditions the range of u remains fairly constant except for u at ST3 and ST1-storm during high-energetic conditions, where u decreases over the tidal cycle. During low-energetic conditions, u varies between -1.3 and 1.3 m/s at the three most seaward measurement locations, located in the shoaling and outer surf zone, and u becomes smaller towards the shore at ST3, located in the inner surf zone. For high-energetic conditions, u ranges between -1.5 and 1.5 m/s. On top of the beachplain, at ST1-storm, u is directed onshore with velocities up to 2 m/s.

During both low- and high-energetic conditions v fluctuates strongly in the shoaling and outer surf zone and become more constant onshore. Furthest offshore, strong fluctuations in v occur due to the presence of shear waves, induced by the outflow of the Slufter channel. The outflow causes alongshore friction between different layers of flow and results in strong jumps in v during the tidal cycle. v ranges between -2 and 0.5 m/s. On top of the beachplain, at ST1-storm, v was mostly northwards directed, indicating flow towards the Slufter channel.

During both low- and high-energetic conditions, flow was mostly directed southwards, but shear waves may change the alongshore current to a northward directed flow.

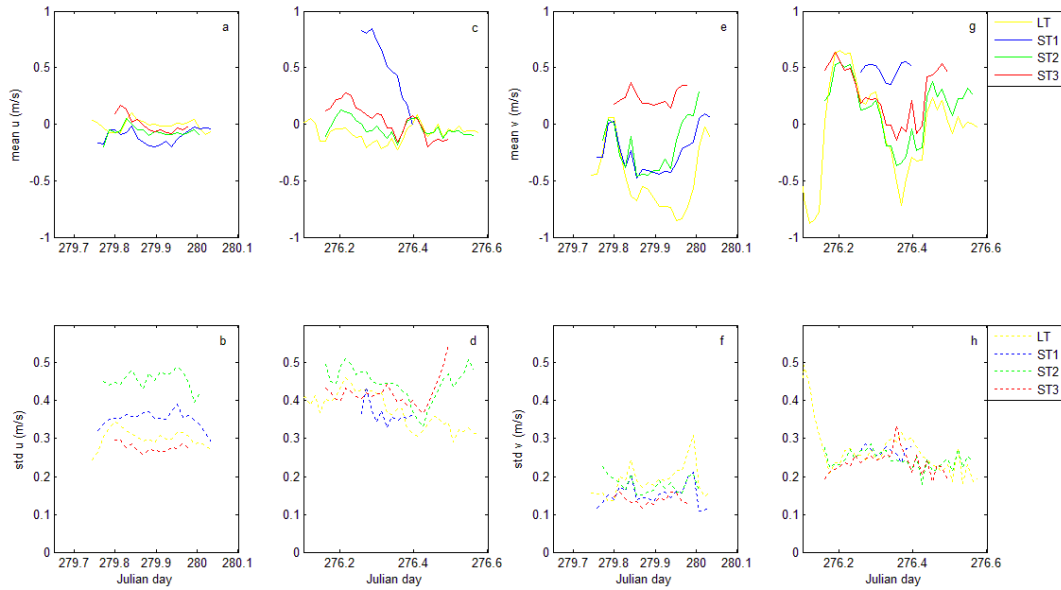


**Figure 21: 20 minute-averaged cross-shore (u) and alongshore (v) and its standard deviation for analyzed tidal cycles: a) u-mean during low-energetic conditions, b) u-std during low-energetic conditions, c) u-mean during high-energetic conditions, d) u-std during high-energetic conditions, e) v-mean during low-energetic conditions, f) v-std during low-energetic conditions, g) v-mean during high-energetic conditions, h) v-std during high-energetic conditions.**

In figure 22, the root mean square cross-shore and alongshore velocities ( $u_{rms}$  and  $v_{rms}$ ) of the low- and high frequency range (lf and hf) are depicted during low- and high-energetic conditions. For both low- and high-energetic conditions,  $u_{rms,hf}$  increases until in the outer surf zone due to shoaling after which  $u_{rms,hf}$  decreases onshore due to high-frequency wave breaking (Figure 22a).  $u_{rms,lf}$  is a factor 3 smaller than  $u_{rms,hf}$  during low-energetic conditions and a factor 2 smaller during high-energetic conditions (Figure 22a&e). During both low- and high-energetic conditions,  $u_{rms,lf}$  increases slowly onshore, indicating shoaling of low-frequency waves onshore (Figure 22e).

$v_{rms,hf}$  is relatively constant in the nearshore and decreases slowly onshore (Figure 22b). The ratio of  $u_{rms,hf}^2/v_{rms,hf}^2$  is between 5-8 smaller in the shoaling and outer surf zone during low-energetic conditions (Figure 22c) and  $u_{rms,hf}^2/v_{rms,hf}^2$  only goes to 1 in the inner surf zone due to a decrease in  $u_{rms,hf}$  due to high-frequency wave breaking. During high-energetic conditions, the ratio of  $u_{rms,hf}^2/v_{rms,hf}^2$  is between 3 and 4 in the shoaling and outer surf zone and decreases to 1 onshore (Figure 22g). The ratio between  $u_{rms,hf}^2/v_{rms,hf}^2$  shows that high-frequency waves are essentially shore-normal in the shoaling zone and the outer surf

zone during low-energetic conditions. During high-energetic conditions,  $v_{rms,hf}$  is larger than during low-energetic conditions.

$v_{rms,lf}$  is of the same magnitude as  $u_{rms,lf}$  in the shoaling and outer surf zone (Figure 22c&f), indicating shore-normal and shore-parallel propagation of low-frequency waves. The shear waves present at the landward side of the measurement transect are reflected in  $v_{rms}$ . During both low- and high-energetic conditions,  $u_{rms}$  becomes more dominant over  $v_{rms}$  in onshore direction (Figure 22c&g) and low-frequency wave propagate in a more shore-normal direction.

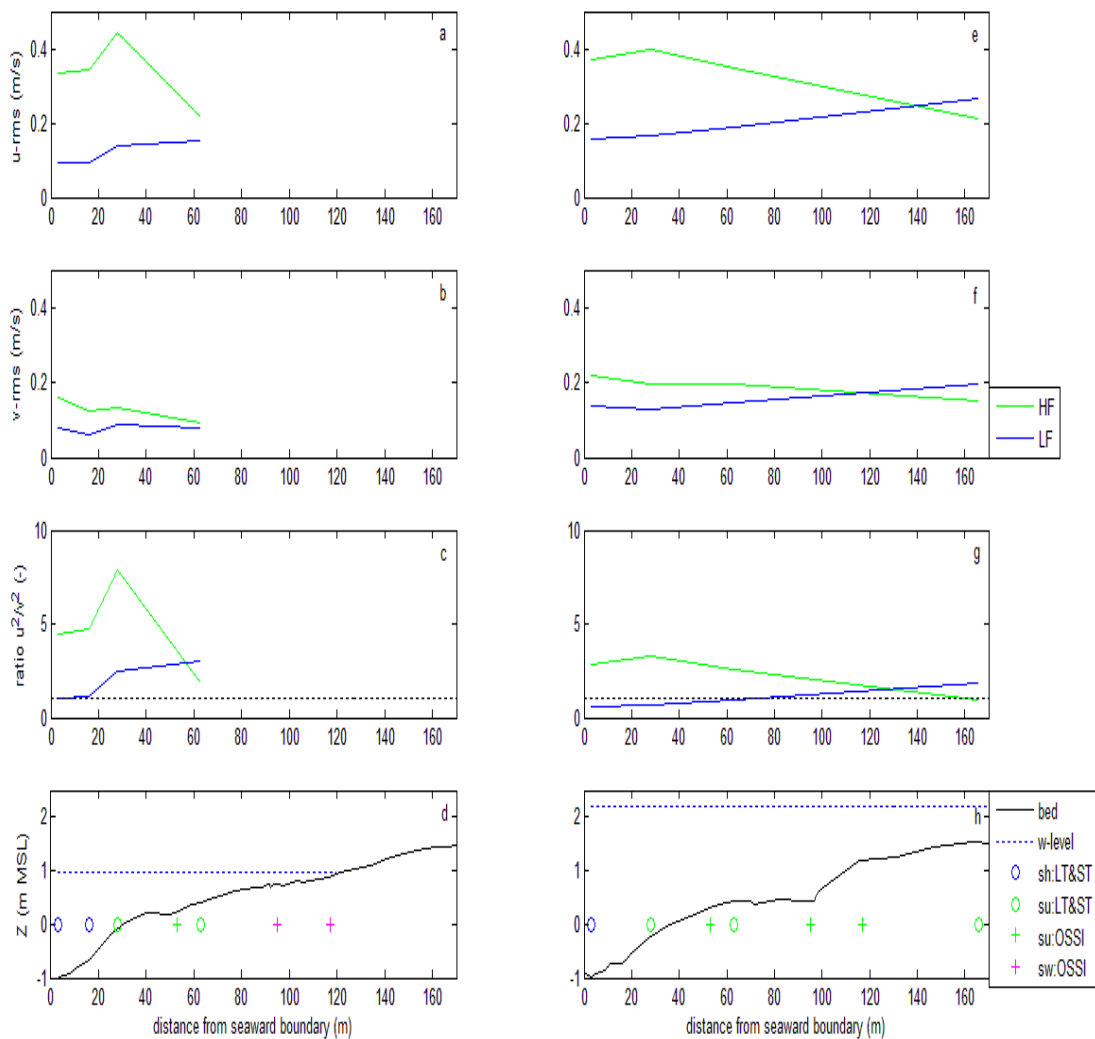


**Figure 22: Cross- and alongshore velocities during high- and low-energetic conditions: a)  $u_{rms}$ , b)  $v_{rms}$ , c) ratio  $u_{rms}^2/v_{rms}^2$ , d) bed profile and location measurement profiles in hydrodynamic zones during low-energetic conditions (sh: shoaling, su: surf and sw: swash zone). e)  $u_{rms}$ , f)  $v_{rms}$ , g) ratio  $u_{rms}^2/v_{rms}^2$ , h) bed profile and location measurement profiles in hydrodynamic zones during high-energetic conditions.**

## 4.2 Relative contribution low- and high-frequency waves during low- and high-energetic conditions

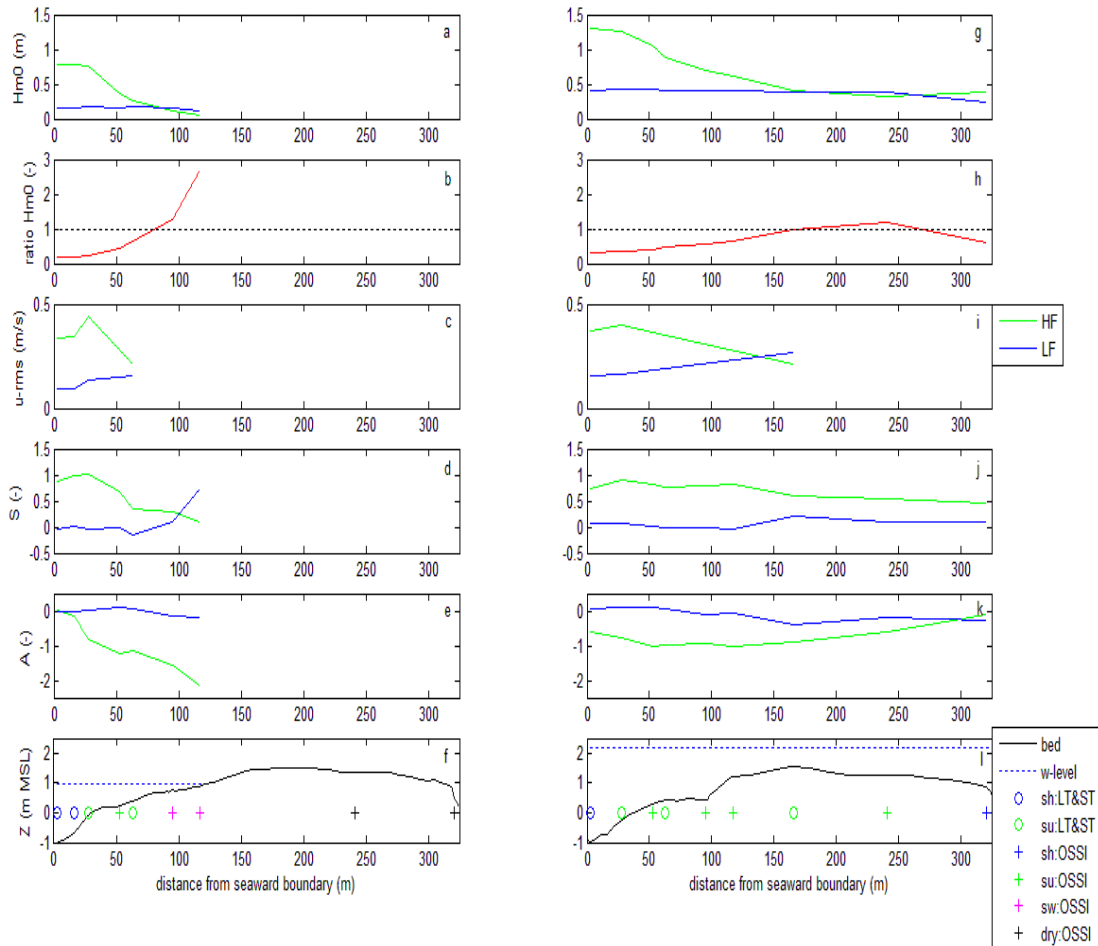


**Figure 23: Wave characteristics of low- and high-frequency ranges: a)  $H_{m0}$ , b) ratio  $H_{m0} (lf)/H_{m0} (hf)$ , c)  $u_{rms}$ , d) Skewness, e) Asymmetry, f) bed profile and measurement locations during low-energetic conditions (sh: shoaling, su: surf, sw: swash zone and dry). : g)  $H_{m0}$ , h) ratio  $H_{m0} (lf)/H_{m0} (hf)$ , i)  $u_{rms}$ , j) Skewness, k) Asymmetry, l) bed profile and measurement locations during high-energetic conditions.**

In figure 23a&b, the  $H_{m0}$  (hf) and  $H_{m0}$  (lf) during low- and high-energetic conditions are depicted. High-frequency waves break in the surf zone, whereas low-frequency waves remain and propagate onshore, shoaling slightly in the inner surf zone. In the swash zone, at Ossi 2 and 3,  $H_{m0}$  (lf) decreases slightly, indicating low-frequency wave dissipation

During high-energetic conditions, the entire beachplain is located in the surf zone.  $H_{m0}$  (hf) decreases until on the top of the beachplain, where water depth is smallest.  $H_{m0}$  (lf) remains constant over the beachplain and interestingly low-frequency waves appear to dissipate at the landward side of the beachplain.

From low- to high-energetic conditions, the magnitude of  $H_{m0}$  (hf) and  $H_{m0}$  (lf) at LT increases with a factor 1.7 and a factor 2.8 respectively. Thus, the increase in  $H_{m0}$  (lf) increases more strongly in the nearshore with increasing  $H_{m0}$  Offshore than the increase in  $H_{m0}$  (hf), which is also reflected in the ratio  $H_{m0}$  (lf)/ $H_{m0}$  (hf) (Figure 23c&d) going from 0.15 to 0.41 at the seaward side of the measurement transect. This corresponds with findings of Butt & Russel (1999) and Aagaard & Bryan (2003).

During low-energetic conditions, the ratio between  $H_{m0}$  (lf)/ $H_{m0}$  (hf) increases onshore and low-frequency wave become dominant over high-frequency waves in the inner surf zone and swash zone. The dominance of  $H_{m0}$  (lf) over  $H_{m0}$  (hf) increases most strongly in the swash zone (Figure 22c) to a value of 2.7. During high-energetic conditions, the ratio  $H_{m0}$  (lf)/ $H_{m0}$  (hf) also increases onshore, but is smaller than during low-energetic conditions. A maximum value of 1.2 is reached on top of the beachplain. At the landward side of the beachplain, infragravity waves appear to dissipate and high-frequency waves become dominant over low-frequency waves again.

During both low- and high-energetic conditions,  $u_{rms,hf}$  increases until in the outer surf zone, after which it decreases onshore due to high-frequency wave breaking (Figure 22c&i). From the outer surf zone,  $u_{rms,lf}$  increases onshore during both low- and high-energetic conditions. It is an indication that the shape of low-frequency waves transforms in the surf and swash zone. Unfortunately, no flow data is present in the swash zone during low-energetic conditions and at the landward side of the beachplain during high-energetic conditions, where low-frequency waves appear to dissipate. During low-energetic conditions,  $u_{rms,lf}$  is one fourth of  $u_{rms,hf}$  at the seaward side of the measurement location. During high-energetic conditions,  $u_{rms,lf}$  is one half of  $u_{rms,hf}$  at the seaward side of the measurement location, corresponding with a stronger increase in low-frequency wave contribution relative to high-frequency wave contribution with increasing  $H_{m0}$  Offshore.

Skewness and asymmetry during low- and high-energetic conditions is only analyzed for the sea surface elevation, or pressure, skewness and asymmetry, because more measurement locations along the cross-shore transect are available with pressure data than with flow velocity data.

High-frequency wave skewness increases in the shoaling and outer surf zone during both low- and high-energetic conditions, resulting in more sharply peaked waves with broad flatten troughs (Figure 22d). Wave breaking results in a decrease in skewness. During high-energetic conditions, the maximum high-frequency wave skewness occurs over a larger cross-

shore distance and extents further onshore due to the increase in water depth as a result of the storm surge. The maximum skewness is approximately 1 for both low- and high-energetic conditions. After wave breaking, the skewness decreases to 0.1 and 0.5 for low- and high-energetic conditions respectively. The difference in skewness in the inner surf zone is also related to the difference in water depth as a result of the storm surge.

High-frequency waves become increasingly negatively asymmetric in the outer surf zone. During low-energetic conditions, high-frequency waves become increasingly asymmetric with decreasing water depth with maximum asymmetry values of -2.1 in the swash zone. During high-energetic conditions, high-frequency asymmetry only reaches a maximum value of -1.0 due to a larger water depth as a result of the storm surge. Maximum asymmetry values are reached seaward and on top of the beachplain. Landward of the beachplain, asymmetry decreases again due to increasing water depth.

Low-frequency skewness fluctuates around 0 in the shoaling and outer surf zone during low-energetic conditions. In the inner surf zone skewness increases strongly to a value of 0.7 in the swash zone, indicating shoaling of low-frequency waves close to the shoreline. During high-energetic conditions, low-frequency skewness reaches a maximum on top of the beachplain, in the smallest water depth, with a value of 0.2. At the landward side of the beachplain, skewness decreases to a value of 0.1. The positive skewness values during low- and high-energetic conditions, indicate low-frequency wave transformation. Low-frequency waves breaking is not expected, since  $H_{m0}(lf)$  remains constant on top of the beachplain.

Low-frequency waves become slightly positively asymmetric (0.1) in the outer surf zone during both low- and high-energetic conditions. During low-energetic conditions, they become negatively asymmetric with a value of -0.2 in the inner surf and swash zone, which might possibly indicate low-frequency wave breaking. During high-energetic conditions, low-frequency waves become negatively asymmetric on top of the beachplain, in the inner surf zone, with a value of -0.4. At the landward side of the beachplain, asymmetry decreases to a value of -0.2. The negative asymmetry on top of the beachplain, indicates low-frequency wave transformation. However, it is not known if the low-frequency waves actually break, since  $H_{m0}(lf)$  remains constant on top of the beachplain and only decreases landward of the top of the beachplain.

Concluding,  $H_{m0}(hf)$  and  $u_{rms}(hf)$  increase in the shoaling zone. The wave shape transforms by becoming more skewed. In the outer surf zone, waves start to break and  $H_{m0}(hf)$  and  $u_{rms,hf}$  decrease in magnitude. The wave shape becomes less skewed after wave

breaking and the wave become asymmetric. High-frequency waves are far less asymmetric during low-energetic conditions than during high-energetic conditions due to a difference in water depth related to the storm surge.

The transformation of the low-frequency wave shape and the small decrease in  $H_{m0}$  (lf) in the swash zone during low-energetic conditions appear to indicate low-frequency wave breaking. Low-frequency waves become increasingly non-linear with decreasing water depth in the inner surf and swash zone.

During high-energetic conditions,  $H_{m0}$  (lf) remains constant until the landward side of the beachplain whereas the low-frequency wave shape transforms already at the seaward side the beachplain with decreasing water depth. Interestingly, low-frequency wave dissipation only occurs at the landward side of the top of the beachplain, where water depth increases again and low-frequency skewness and asymmetry also decrease. It is clear that low-frequency waves transform in the inner surf and swash zone with decreasing water depth during both low- and high-energetic conditions, but if low-frequency waves transformation actually results in breaking requires further investigation.

In the nearshore, low-frequency waves become more dominant over high-frequency waves with decreasing water depth and with increasing  $H_{m0}$  Offshore. During low-energetic conditions, the ratio  $H_{m0}$  (lf)/ $H_{m0}$  (hf) has a value of 2.7 in the swash zone, whereas during high-energetic conditions, the ratio has a value of 1.2 on top of the beachplain.

### 4.3 Spectral analysis

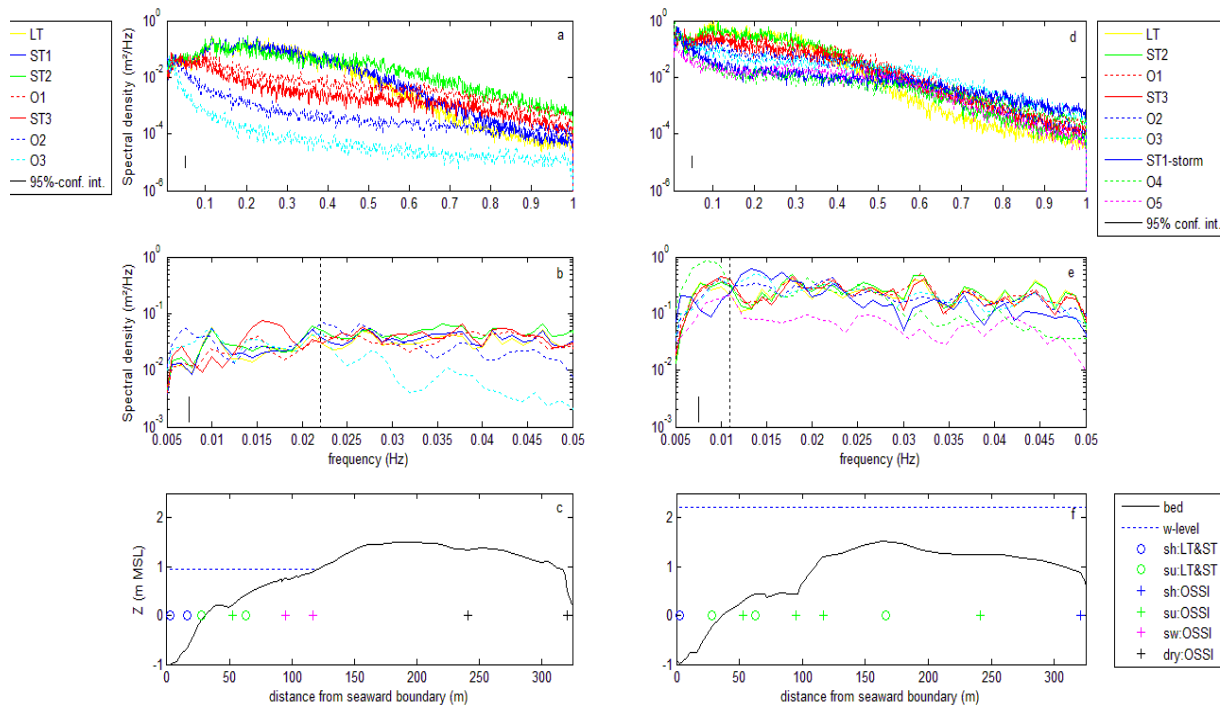


**Figure 24:** Spectral densities of the total frequency range (a) and of the low-frequency range (b) during low-energetic conditions and bed profile and measurement locations (c). Spectral densities of the total frequency range (d), of the low-frequency range (e) during high-energetic conditions and bed profile and measurement locations (f).

In figure 24, the total and low-frequency wave spectra during low- and high-energetic conditions are depicted. Above 0.4 Hz, the spectral density increases onshore, but is expected to not be related to high-frequency wave behaviour. The wave period is too small and it is more likely that the spectral density above 0.4 Hz is related to turbulence motions. Therefore, the upper boundary of the high-frequency range is 0.4 Hz for both low- and high-energetic conditions.

During low-energetic conditions, the spectral density in the high-frequency range (0.05-0.4 Hz) remains constant in the shoaling and outer surf zone (LT until ST2), which corresponds with findings from the previous section. In the inner surf and swash zone (Ossi 1 until Ossi 3), the high-frequency spectral density decreases due to high-frequency wave dissipation (Figure 24a). From ST2 to Ossi 1/ST3, the spectral density decreases simultaneously for almost the entire high-frequency range (0.085-0.4 Hz). From ST3 to Ossi 2, the spectral density decreases until in the low-frequency range for frequencies larger than 0.032 Hz (Figure 24a&b). During high-energetic conditions, the spectral density in the high-

frequency range also decreases simultaneously in the inner surf zone (ST2 until Ossi 5) for the entire high-frequency range (0.05-0.4 Hz).

During low-energetic conditions, the spectral density in the low-frequency range remains constant in the inner surf zone. The spectral density of the higher low-frequency range decreases in the swash zone (Ossi 2 and 3), indicating low-frequency dissipation. This corresponds with findings from section 4.2. The spectral density of the lower low-frequency range does not decrease in the swash zone. The boundary between low-frequency wave dissipation is at 0.022 Hz. During high-energetic conditions, the spectral density of the low-frequency range remains constant in the surf zone and the spectral density of the upper low-frequency range (0.011-0.05 Hz) decreases at Ossi 4 and 5, at the landward side of the beachplain located in the inner surf zone.

During both low- and high-energetic conditions, low-frequency dissipation occurs for the upper low-frequency range, but the location differs strongly.

Raubenheimer et al. (1996) found that dissipation of low-frequency waves is small and reflection is large, which does not correspond with findings at the Slufter. Spectral analysis shows that dissipation occurs, especially for the higher low-frequency domain. Dissipation occurs for a larger low-frequency range (0.011-0.05) during high-energetic conditions than during low-energetic conditions (0.022-0.05).

During low- and high-energetic conditions, indications for a cross-shore progressive or partial standing infragravity wave pattern are present (Figure 24b&e). A cross-shore standing infragravity wave pattern is characterized by minima and maxima in the spectra which occur at the same frequency for measurement locations located relatively far away from each other, whereas nearby measurement locations have minima and maxima coinciding at similar frequencies. During low-energetic conditions, no such a pattern is found for the higher low-frequency range and a more irregular distribution of maximum and minimum spectral densities is present. The higher and lower low-frequency range suggests a progressive and (possible) partial cross-shore standing infragravity respectively. During high-energetic conditions, a progressive cross-shore infragravity wave pattern is suggested.

Based on the absence of any significant low-frequency peaks and lows (node/anti-node pattern) in the spectra and the occurrence of low-frequency wave dissipation in the swash during low-energetic conditions, it is expected that reflection at the shoreline is smaller than 100%. In the next section the cross-shore infragravity wave pattern is investigated more thoroughly by means of analyzing phase difference and coherence between the measurement locations and by analyzing low-frequency energy fluxes.

#### 4.4 Phase difference analysis

In figure 25, the measured and predicted phase difference and the coherence of the sea surface elevation between the most seaward measurement location, LT, and the other measurement locations during low-energetic and high-energetic conditions is depicted. The number of degrees of freedom are 28 for the measured phase difference and coherence, the spectral resolution is 0.0011 Hz and the 95% confidence interval for the lower and upper boundary is 0.63 and 1.83, but is not depicted in figure 25 to optimize the clarity of the figure.

The gradient of the phase difference in the low-frequency range is constant (Figure 25d&k), indicating that the waves travel with the same velocity. Therefore, the predicted phase difference can be computed. The predicted phase difference  $\varphi$  ( $\pi$ ) for each frequency is computed by using the wave celerity  $c$  (m/s)

$$c = \sqrt{gh}, \quad (14)$$

and

$$\varphi = \frac{\Delta X}{c} * \frac{\pi}{T_f}, \quad (15)$$

where  $h$  and  $\Delta X$  are the mean water depth (m) and the distance (m) between the measurement locations respectively,  $g$  is the gravitational constant ( $9.81 \text{ m/s}^2$ ) and  $T_f$  the wave period of each frequency ( $T = 1/f$  (s)).  $\Delta X/c$  represents the time required for the wave to travel between measurement locations.

The predicted  $\varphi$  of the high-frequency spectrum (0.05-0.04) is of a similar magnitude as the measured  $\varphi$ , before wave breaking during both low- and high-energetic conditions. High-frequency wave breaking results in a disconnection of the wave at that frequency with the wave group velocity and the measured  $\varphi$  does not correspond with the predicted  $\varphi$  anymore. During, high-energetic conditions, the seaward boundary of the surf zone is located further offshore, resulting in an earlier disconnection of the waves in the high-frequency range with the group celerity and a larger discrepancy between measured and predicted  $\varphi$  is observed further onshore. During high-energetic conditions, the gradient of the predicted phase difference is smaller than during low-energetic conditions. An increase in water depth results in an increase in  $c$ , resulting in  $\Delta X/c$  and  $\varphi$  being smaller.

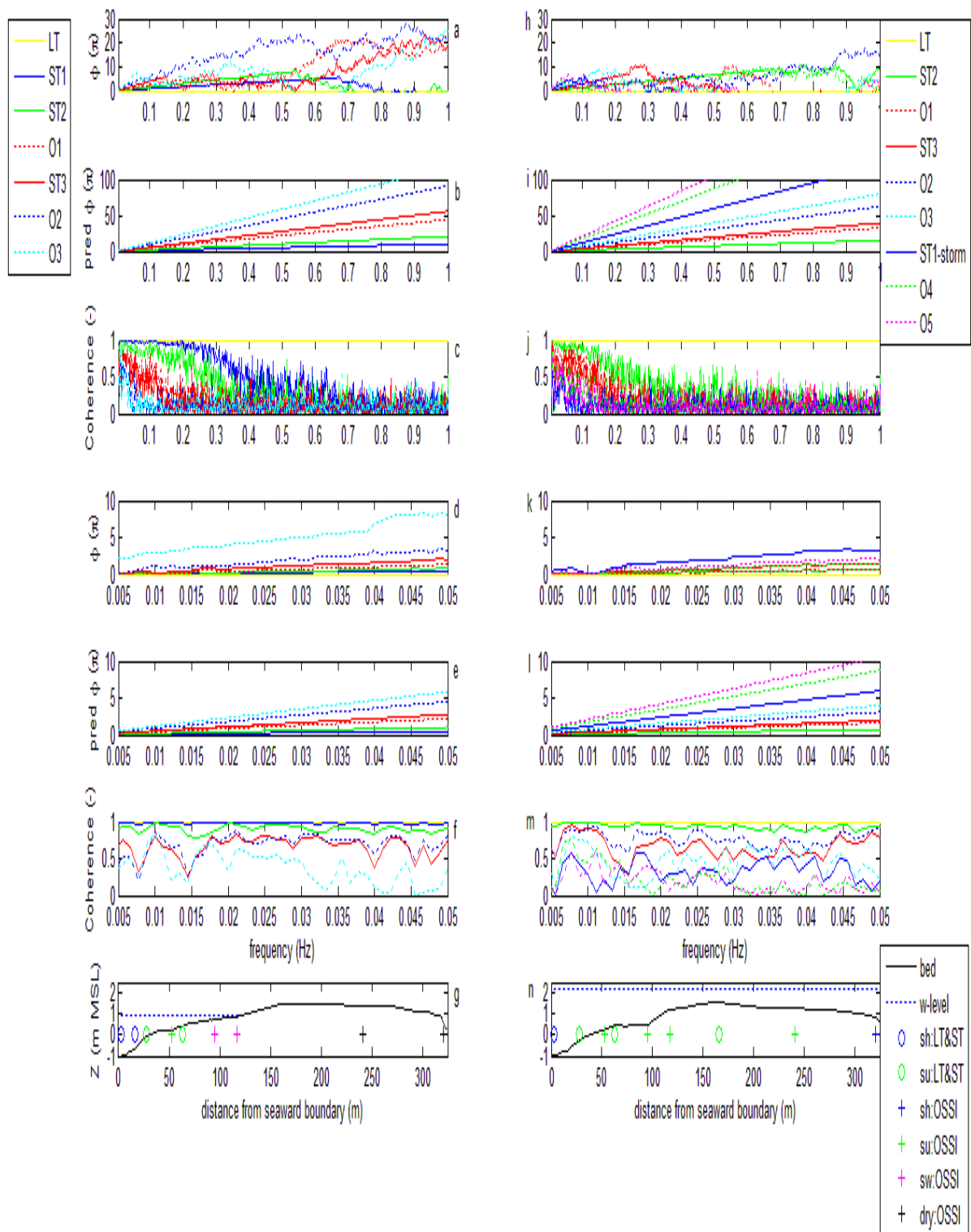


**Figure 25: Phase differences (a), predicted phase differences (b) and coherence (c) of total frequency range during low-energetic conditions. Phase differences (d), predicted phase differences (e) and coherence (f) of low-frequency range during low-energetic conditions. Phase differences (h), predicted phase differences (i) and coherence (j) of total frequency range during high-energetic conditions. Phase differences (k), predicted phase differences (l) and coherence (m) of low-frequency range during high-energetic conditions. Beach profile and measurement locations during low- (g) and high-energetic conditions (n).**

Figure 25a&h show that in the high-frequency range,  $\phi$  increases with a constant gradient with increasing frequency and increasing  $\Delta X$  until in the outer surf zone. During low-energetic conditions, the constant gradient disappears for the high-frequency range in the inner surf zone, from ST2 to Ossi 1. At ST3,  $\phi$  does not increase with a constant gradient for frequencies above 0.15 Hz (Figure 25a). In the swash zone, at Ossi 3, the boundary below which  $\phi$  increases with a constant gradient is located in the low-frequency range at 0.04 Hz. The coherence decreases already before the constant gradient disappears. The coherence in the high-frequency range shows already a strong drop above 0.35 Hz in the shoaling zone and the coherence drops further for the entire high-frequency range in the outer surf zone (ST2) and drops even more in the inner surf zone (ST3) (Figure 25c). The decrease in coherence and the disappearance of the constant gradient indicates strong wave transformation and wave breaking also supported by the spectral analysis and the trends witnessed in high-frequency wave skewness and asymmetry.

During high-energetic conditions, the measured  $\phi$  shows a similar trend as during low-energetic conditions (Figure 25h). The coherence drops at a more seaward location due to a seaward shift of the seaward surf zone boundary (Figure 25j).

During low-energetic conditions, the measured  $\phi$  of low-frequency waves also increases with a constant gradient with increasing frequency and increasing  $\Delta X$  (Figure 25d). Only in the swash zone, the constant gradient is disturbed between 0.04 and 0.05 Hz. The coherence for the low-frequency range during low-energetic conditions drops slightly in the shoaling and outer surf zone until ST2 and then drops more strongly in the inner surf zone, from ST3 on (Figure 25f). In the swash zone, at Ossi 3, the coherence has dropped most strongly at the higher-frequencies of the low-frequency range. The phase difference and coherence indicate the presence of a progressive infragravity wave pattern under low-energetic conditions rather than a standing infragravity wave pattern. Also, the low-frequency wave transformation and breaking in the inner surf and swash zone observed in section 4.2 and 4.3 is supported by the trends in phase difference and coherence (Figure 25d&f).

During high-energetic conditions, a cross-shore progressive infragravity wave pattern is also present at the Slufter. At 0.01 Hz,  $\phi$  drops close to 0 for ST1-storm, Ossi 4 and 5. At 0.015 Hz,  $\phi$  increases again with a constant gradient for the mentioned measurement locations (Figure 25k). However,  $\phi$  of Ossi 4 and 5 remains significantly smaller than the predicted  $\phi$  and the measured  $\phi$  of ST1-storm. The drop in  $\phi$  at 0.01 Hz and the discrepancy in the constant trend for the upper low-frequency range indicates wave transformation on top and landward of the beachplain. The coherence of the low-frequency range during high-energetic

conditions drops strongly twice in the inner surf zone at ST3 and ST1-storm and is smaller than during low-energetic conditions for Ossi 4 and 5, which are located at the landward side of the beachplain (Figure 25m). Together, the phase difference and coherence indicate that for low-frequency waves transform on top and at the landward side of the beachplain, for almost the entire low-frequency range with a boundary at 0.011 Hz. This boundary corresponds with the decrease in spectral density of the low-frequency range found in the previous section.

The progressive infragravity wave pattern found at the Slufter contradicts with other studies. Guza & Thornton (1985) found a cross-shore standing infragravity wave pattern in the nearshore area for several beaches (beach slopes between 0.022-0.062), Masselink (1995) (beach slope between 0.015-0.035) and Henderson et al. (2001) (beach slope between 0.01-0.1) found a cross-shore infragravity wave structure close to the shoreline, which becomes partially standing or progressive further offshore due to dissipation. Generally the beach slope increases onshore, where at the Slufter the strongest low-frequency dissipation occurred. At the Slufter, the beach slope is 0.015 which is small compared to the other beaches. The small slope is a possible explanation for low-frequency dissipation at the Slufter which decreases the rate of low-frequency wave reflection at the shoreline.

Sheremet et al. (2002) state that the cross-shore infragravity wave pattern depends on the amount of forcing and damping and the rate of shoreline reflection based on analysis of the low-frequency energy fluxes. Sheremet et al. (2002) state that only a partial cross-shore standing infragravity wave pattern can form in the nearshore area since it is thought that the cross-shore amplitude variations of the shoreward and seaward propagating low-frequency waves differ due to low-frequency wave dissipation. Furthermore, Elgar et al. (1997) found that onshore- and offshore-directed low-frequency components are not in phase, resulting in no significant resonance interactions and only a (possible) partial cross-shore standing infragravity wave pattern. The conditions for a cross-shore progressive infragravity wave pattern present at the Slufter are relatively strong forcing and damping. During low-energetic conditions, low-frequency wave forcing is smaller than during high-energetic conditions, but wave damping is strong, especially in the swash zone. During high-energetic conditions, low-frequency waves travel over the beachplain and reflection is expected to be minimal. In the next section, the cross-shore infragravity wave pattern and the rate of reflection is examined by analyzing the energy fluxes.

## 4.5 Energy fluxes

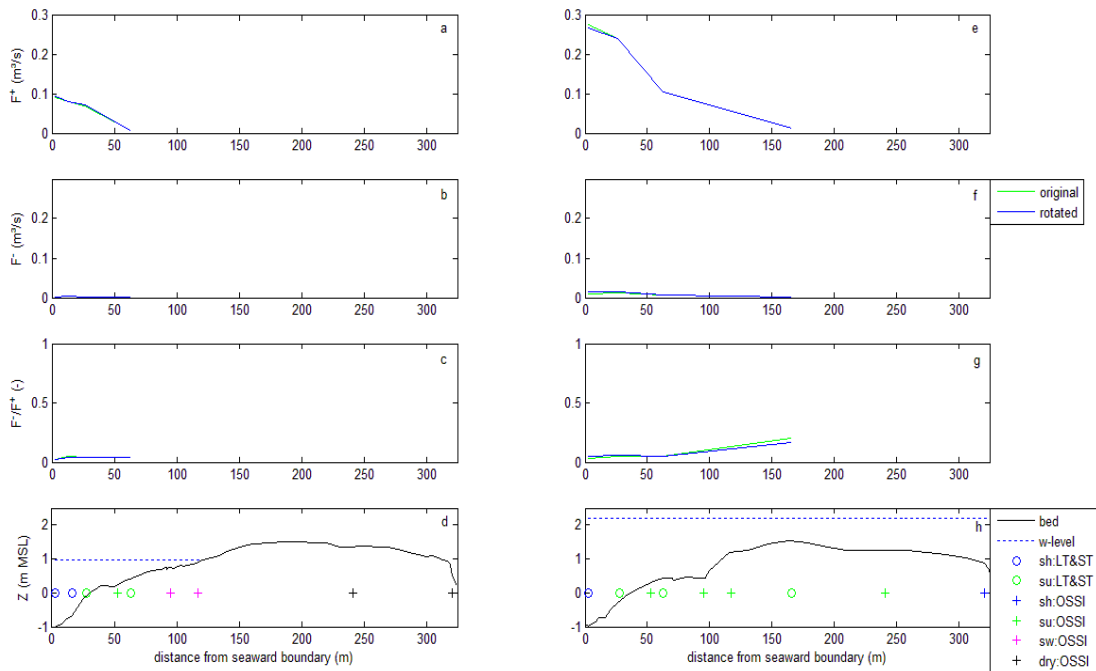


**Figure 26: Bulk onshore (a) and offshore (b) high-frequency energy fluxes (0.05-0.4 Hz) and (c) bulk high-frequency reflection coefficient during low-energetic conditions and (d) bed profile and measurement locations. Bulk onshore (e) and offshore (f) high-frequency energy fluxes and (g) bulk high-frequency reflection coefficient during high-energetic conditions and (h) bed profile and measurement locations.**

Fluxes are computed for both the low- and high-frequency domain. The coherence of high-frequency waves decreases above 0.4 and 0.3 Hz for low- and high-energetic conditions respectively (Figure 25) and frequencies larger than 0.4 Hz are not related to high-frequency wave dissipation (Figure 24). Therefore, the upper boundary of the high-frequency domain is set at 0.4 Hz. Fluxes are computed based on the original velocity signal and based on the rotated velocity signal. Of the latter, the cross-shore velocities are directed shore-normal.

During low- and high-energetic conditions, the onshore high-frequency energy flux ( $F^+$  (hf)) decreases in the surf zone due to high-frequency wave breaking (Figure 26). The offshore high-frequency flux ( $F^-$  (hf)) is much smaller than  $F^+$  (hf) and decrease onshore during both low- and high-energetic conditions. The bulk high-frequency reflection coefficient ( $R^2$ ), which is the ratio between  $F^-$  and  $F^+$ , is small with a constant value (0.05) during low-energetic conditions and  $R^2$  is between 0.05-0.2 during high-energetic conditions increasing onshore. The increase is related to the division of two very small numbers with each other, where a small difference in  $F^+$  (hf) and  $F^-$  (hf) already results in a large variation in  $R^2$ .  $F^+$  (hf) and  $F^-$  (hf) increase by a factor 3 from low- to high-energetic conditions.

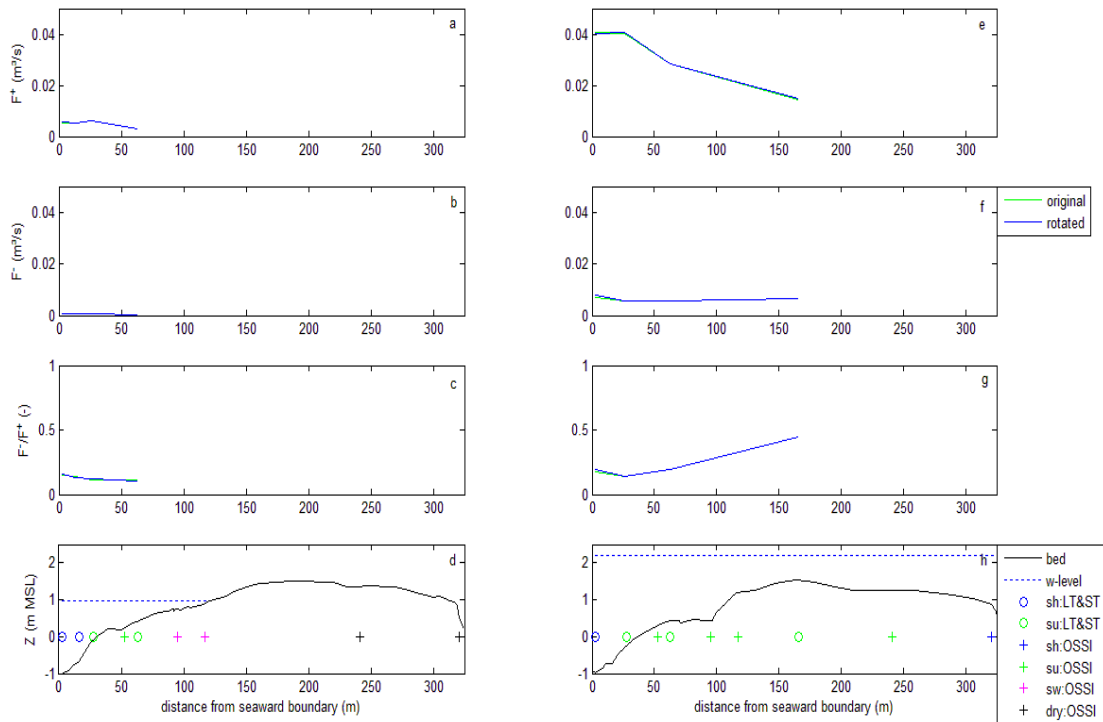


**Figure 27: Bulk onshore (a) and offshore (b) infragravity energy fluxes (0.005-0.05 Hz) and (c) bulk infragravity reflection coefficient during low-energetic conditions and d) bed profile and measurement locations. Bulk onshore (e) and offshore (f) infragravity energy fluxes (0.005-0.05 Hz) and (g) bulk infragravity reflection coefficient during high-energetic conditions and h) bed profile and measurement locations.**

$F^+$  (lf) increases with a factor 7.5 from low- to high-energetic conditions. Just as  $F^+$  (hf),  $F^+$  (lf) decreases onshore, indicating low-frequency dissipation (Figure 27). During low-energetic conditions,  $F^+$  (lf) increases in the shoaling zone (LT to ST1). This trend corresponds with findings from Sheremet et al. (2002) who related the increase in  $F^+$  (lf) in the shoaling zone to nonlinear interaction of onshore propagating low-frequency waves with sea and swell groups. During high-energetic conditions, the shoaling zone is located seaward of the measurement location and no conclusions can be drawn concerning the energy fluxes in the shoaling zone. During high-energetic conditions,  $F^+$  (lf) decreases strongly between  $x=30$  and  $x=70$  m, in the outer surf zone. It is an indication that high-frequency wave breaking might strongly influence low-frequency dissipation during more energetic conditions as also found by Herbers et al. (1995) and Ruessink (1998a&b).

During low-energetic conditions,  $F^-$  (lf) decreases in the inner surf zone, whereas during high-energetic conditions  $F^-$  (lf) remains constant in the surf zone. Sheremet et al.

(2002) found  $F^-$  ( $lf$ ) to increase in magnitude inside the surf zone related to low-frequency wave reflection, which is not found at the Slufter.

At the Slufter,  $R^2$  has a value of 0.1 during low-energetic conditions and a value between 0.1-0.45 during high-energetic conditions, increasing onshore. The increase in  $R^2$  during high-energetic conditions is related to  $F^-$  ( $lf$ ) remaining constant in the surf zone, whereas  $F^+$  ( $lf$ ) decreases. The small  $R^2$  values indicate that almost no low-frequency wave reflection at the shoreline occurs. Based on the spectral analysis, it is expected that reflection would occur mostly for the lower low-frequency range, since for the upper low-frequency range dissipation occurs.

The small  $R^2$  values found close to the shoreline at the Slufter support the evidence from the previous sections that a cross-shore progressive infragravity wave pattern is present at the Slufter. Sheremet et al. (2002) found at the Duck beach in North Carolina, with an average beach slope of 0.02, larger  $R^2$  values than at the Slufter.  $R^2$  increased to a value of approximately 1 in the surf zone. Van Dongeren et al. (2007) mention that the beach slope at Duck at the shoreline is much larger than the average beach slope, being 0.05. The difference in beach slopes is a likely explanation for the difference in  $R^2$  values at Duck and the Slufter. It shows that large-scale beach bathymetry close to the shoreline is important factor determining the reflection of low-frequency wave.

A difference between this study and the study of Sheremet et al. (2002) is that Sheremet et al. (2002) has done measurements between 150 and 500 m from the shoreline. As a result most measurements locations are in the shoaling and outer surf zone. At the Slufter, measurements were done between 60 and 120 m from the shoreline during low-energetic (normal beach) conditions with all measurement locations being in the surf zone.

In figure 28, the alongshore energy flux of the low- and high-frequency ranges (0.005-0.05 and 0.05-0.4 Hz) are depicted.  $F^+$  and  $F^-$  are directed in northern and southern direction respectively. Before rotation of the flow field, the value of  $R^2$  is larger than 1, indicating that the flow is mostly directed in southern direction. This makes sense, since during the low-energetic conditions, wave direction was northwest. After rotation of the flow field,  $F^+$  and  $F^-$  are much smaller and of the same magnitude and  $R^2$  is approximately 1.

During high-energetic conditions, wave direction was southwest, which corresponds with a value of  $R^2$  smaller than 1 found at LT and ST2. Further onshore, the alongshore flux is directed in southward direction ( $R^2 = 2$ ), indicating complex flow patterns over the beachplain. After rotation of the flow field, the alongshore fluxes are approximately 1, except

at the LT. The alongshore energy fluxes indicate that the assumption of shore-normal propagation is only valid after rotation of the flow field.

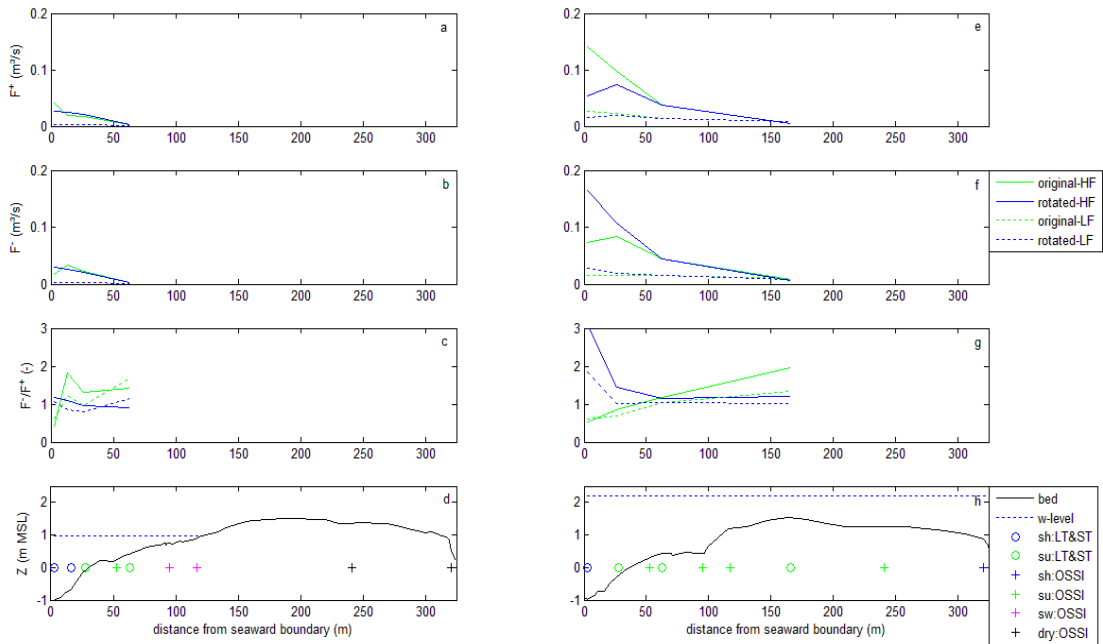


**Figure 28: Bulk northward-,  $F^+$ , (a) and southward-directed,  $F^-$ , (b) low- and high-frequency energy fluxes (0.005-0.05 Hz, 0.05-0.4 Hz) and (c) bulk infragravity reflection coefficient during low-energetic conditions and d) bed profile and measurement locations. Bulk northward-,  $F^+$ , (e) and southward-directed,  $F^-$ , (f) low- and high-frequency energy fluxes and (g) bulk infragravity reflection coefficient during high-energetic conditions and h) bed profile and measurement locations.**

## 5. Discussion: Dissipation mechanisms

The progressive cross-shore infragravity wave pattern at the Slufter during low-energetic, normal beach, conditions, contradicts with other studies (Guza & Thornton, 1985; Masselink, 1995; Henderson et al., 2001; Sheremet et al., 2002) who found a (partial) cross-shore standing infragravity wave pattern. Sheremet et al. (2002) state that the cross-shore infragravity wave pattern depends on the amount of forcing, dissipation and the rate of shoreline reflection. Dissipation of low-frequency waves can be caused by bed friction or high-frequency wave-induced turbulence (Herbers et al., 1995; Ruessink, 1998a; Sheremet et al., 2002; Henderson & Bowen, 2002). Also, dissipation due to nonlinear triad interactions in the surf zone is a possible mechanism (Henderson et al., 2006; Thomson et al., 2006). Van Dongeren et al. (2007) found that on a mild-sloped beach, low-frequency wave dissipation is dominated by low-frequency wave breaking.

Many different mechanisms for low-frequency wave dissipation are presented in literature and there still is much debate concerning the relative contribution of each mechanism in the nearshore. It is outside the scope of this research to determine the relative contribution of each mechanism on low-frequency wave dissipation at the Slufter, but several mechanisms are investigated to get a feel of possible causes of low-frequency wave dissipation at the Slufter. The parametric wave propagation and dissipation model of Battjes & Janssen (1978) as described in van Dongeren et al. (2007) is used to investigate the relative contribution of low-frequency wave dissipation due to bed-friction and low-frequency wave breaking. The model is based on the following equations

$$\frac{d}{dx} \left( \sqrt{gh} \frac{1}{8} \rho g H^2_{rms,fr} \right) = -D_{bot} - D_{br}, \quad (16)$$

$$D_{bot,fr} = f_{cw,fr} \rho \left( \frac{g}{h} \right)^{\frac{3}{2}} \frac{H_{rms,fr}}{\sqrt{8}} \frac{H^2_{rms,fr}}{8}, \quad (17)$$

$$D_{br,fr} = \alpha_{br} f_{fr} \rho g Q_{b,fr} \frac{H^2_{rms,fr}}{4}, \quad (18)$$

where  $d/dx$  is the change in wave energy in the cross-shore direction,  $g$  is the gravitational constant ( $9.81 \text{ m/s}^2$ ),  $h$  is the water depth (m),  $\rho$  is the density of water ( $1030 \text{ kg/m}^3$ ),  $H^2_{rms,fr}$  is

the root mean square wave height of a specified frequency range,  $D_{bot,fr}$  and  $D_{br,fr}$  are the dissipation of wave energy due to bottom friction and wave breaking respectively of the specified frequency range (J/m/s).  $f_{cw,fr}$  is the wave-related friction coefficient of the specified frequency range which is a function of the semi-excursion length of the orbital motion at the bed and a roughness length  $k_s$ . A  $k_s$  value of 0.1 m and 0.25 m is taken for low- and high-energetic conditions respectively, based on observations in the field.  $\alpha_b$  is a parameter with a value of 1,  $f_{fr}$  is the radial frequency of a specified frequency range and  $Q_{b,fr}$  is the percentage of broken waves in the specified frequency range at a certain location as a function of the maximum wave height ( $H_{max,fr}$ ) and  $H_{rms,fr}$ .

An indicator for the rate of low-frequency wave dissipation at the beach, is the normalized beach slope. Battjes et al. (2004) found that shoaling of the incoming low-frequency wave and reflection of the low-frequency waves at the shoreline is a function of the normalized slope parameter  $\beta_s$

$$\beta_s = \frac{h_x}{\omega} \sqrt{\frac{g}{h_s}}, \quad (19)$$

where  $h_x$  is the beach slope (-),  $\omega$  is the radial frequency of the defined low-frequency spectrum (fr) ( $s^{-1}$ ) and  $h_s$  is a representative shoaling depth of the defined fr (m).

	Mod					Storm			
FR	freq range (Hz)	T (f) (s & Hz)	h-s (m)	Beta-s (-)	FR	freq range (Hz)	T (f) (s & Hz)	h-s (m)	Beta-s (-)
1)	0.035-0.05	23 (0.044)	1.95-1.35	0.13-0.14	1)	0.03-0.05	24 (0.042)	3.15-2.4	-
2)	0.022-0.035	34 (0.029)	1.95-1.35	0.19-0.20	2)	0.011-0.03	50 (0.02)	3.15-2.4	-
3)	0.005-0.022	100 (0.01)	1.95-1.35	0.55-0.6	3)	0.005-0.011	130 (0.077)	3.15-2.4	-

**Table 5: frequency range (Hz), radial wave period (s) of each frequency range, range of representative shoaling depth (m) of each frequency range and normalized bed slope of each frequency range during low- and high-energetic conditions. Slope during low- and high-energetic conditions is 0.0155 and -0.0033 respectively.**

In table 5, the values of  $\beta_s$  for the different low-frequency ranges are given. Battjes et al. (2004) makes a distinction between mild-slope ( $\beta_s < 0.06$ ) and steep-slope regimes ( $\beta_s > 0.3$ ), where the amplitude growth in the shoaling zone is large (small) and reflection at the shoreline is small (larger) for the mild- (steep-) slope regime. Battjes et al. (2004) already

remark that the boundaries of  $\beta_s$  are tentative, since they are based on a single (laboratory) dataset. Deviations in the boundaries may be present under different conditions.

Also, there is no clear definition of the characteristic shoaling depth, which makes this parameter subjective. Therefore, instead of using a single characteristic water depth, a range in characteristic water depth is used.

In the Slufter, 3 distinct ranges in the low-frequency spectrum during low- and high-energetic conditions are distinguished based on spectral analysis (FR 1, 2 and 3 in table 5). During low-energetic conditions, low-frequency waves between 0.035-0.05 Hz (1) and 0.022-0.035 Hz (2) dissipate at Ossi 2 and 3 respectively. Low-frequency waves between 0.005-0.022 Hz (3) do not dissipate. During high-energetic conditions, low-frequency waves between 0.03-0.05 Hz (1) and of 0.011-0.03 Hz (2) dissipate at Ossi 4 and Ossi 5 respectively. Low-frequency waves between 0.005-0.011 Hz (3) do not dissipate. The representative shoaling depth,  $h_s$ , is based on visual analysis of the  $H_{rms,fr}$  (Figure 29a&b). During high-energetic conditions,  $\beta_s$  can not be computed, since normal beach conditions are not present. Water depth increases onshore and de-shoaling occurs. The slope at the landward side of the beachplain is negative and very small, resulting in small (negative values) of  $\beta_s$ , theoretically placing it in the mild-slope regime ( $\beta_s < 0.06$ ).

During low-energetic conditions,  $\beta_s$  is between the mild- and steep-slope regime for FR (1) and (2), where FR (3) is in the steep-slope regime, indicating possible low-frequency dissipation for FR (1) and (2) and strong shoreline reflection for FR (3). As mentioned, the boundaries of  $\beta_s$  may deviate under different conditions. The decrease in spectral density for FR (1) and (2) indicates that FR (1) and (2) have mild-slope regime characteristics, whereas the spectral density of FR (3) remains constant in the nearshore, indicating shoreline reflection.

In figure 29, the measured and modelled  $H_{rms,fr}$ ,  $D_{bot,fr}$  and  $D_{br,fr}$  are depicted during low- and high-energetic conditions. During low-energetic conditions, the modelled  $H_{rms}$  fits well with the measured  $H_{rms}$  of each frequency range (Figure 29a). Only in the swash zone, the modelled  $H_{rms}$  overestimates. For a  $k_s$  of 0.15 m, modelled  $H_{rms}$  fit better with the measured  $H_{rms}$ , but such a larger  $k_s$  value is not thought realistic. Other dissipation mechanisms or uncertainties in the parameter input of the model, such as the estimation of the water depth close to the shoreline and  $k_s$ , might explain this discrepancy.

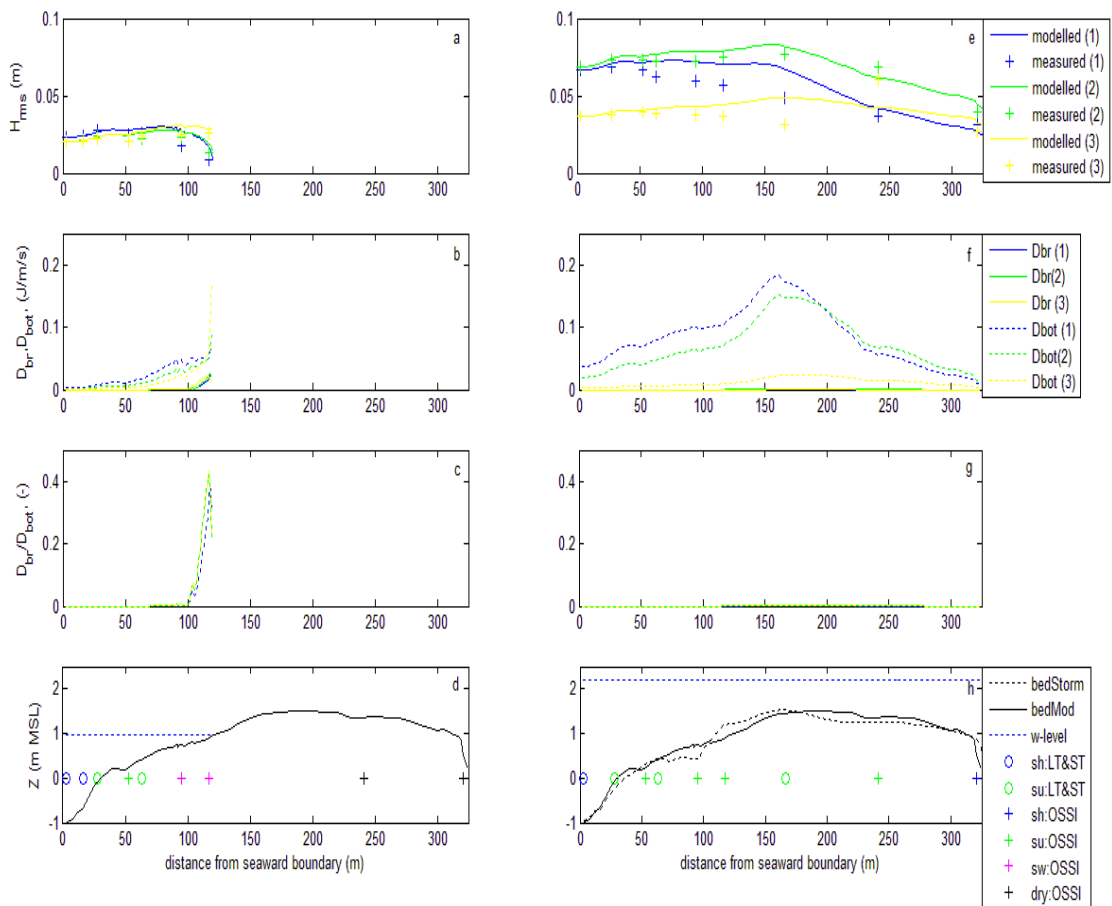


**Figure 29: a) measured and modelled  $H_{rms,fr}$ , b)  $D_{bot}$  and  $D_{br}$ , c) the ratio of  $D_{br}/D_{bot}$  of each frequency range during low-energetic conditions. e) measured and modelled  $H_{rms,fr}$ , f)  $D_{bot}$  and  $D_{br}$ , g) the ratio of  $D_{br}/D_{bot}$  of each frequency range during high-energetic conditions. d) and h) bed profile and measurement locations during low- and high-energetic conditions respectively.**

In the shoaling and surf zone,  $H_{rms}$  (1) is larger than  $H_{rms}$  (2 and 3) during low-energetic conditions. In the swash zone,  $H_{rms}$  (1) decreases most seaward and most strongly.  $H_{rms}$  (2) also decreases, whereas  $H_{rms}$  (3) shoals in the swash zone and only decreases slightly in magnitude, which corresponds with the relative values of  $\beta_s$  (table 5). However,  $H_{rms}$  (3) does dissipate due to bed friction and wave breaking close to the shoreline (Figure 29b). Based on the model results, dissipation of FR (1) and (2) is mostly caused by bed friction (Figure 29 b&c). Low-frequency wave breaking only occurs very close to the shoreline ( $x > 115$  m) for all frequency ranges, whereas low-frequency wave dissipation due to bed friction occurs along the entire cross-shore profile. Close to the shoreline, low-frequency wave dissipation due to bed friction is a factor 2.5 larger than low-frequency wave dissipation due to low-frequency wave breaking. These findings contrast with findings from van Dongeren et al. (2007) who found that low-frequency wave dissipation was strongly dominated by low-

frequency wave breaking for bichromatic wave conditions in a flume with a slope of 0.0286. The slope is a factor 1.8 steeper than the slope at the Slufter which might be a possible explanation for the different relative contribution of both dissipation mechanisms. However, the normalized bed slope was smaller in the flume than at the Slufter. A more likely explanation is the scale difference. In the flume, low-frequency waves with similar wave periods and lengths as in the Slufter propagate over a 24.5 m cross-shore distance, whereas low-frequency waves propagate over a 120 m cross-shore distance in the nearshore. The total dissipation due to bed friction is already much larger along this transect. The decrease in  $H_{\text{rms,fr}}$  due to bed friction results in low-frequency wave breaking further onshore, since the fraction of breaking waves,  $Q_b$ , which depends on the ratio between  $H_{\text{rms,fr}}$  and  $H_{\text{max,fr}}$ , is smaller. Also, the variability of a wave train under natural conditions is larger than for a bichromatic wave group. This can lead to a lower  $H_{\text{rms,fr}}$  which contributes to an even smaller value of  $Q_b$ .

During high-energetic conditions, the modelled  $H_{\text{rms}}$  (1) and (3) are overestimated, whereas  $H_{\text{rms}}$  (2) fits well with the measured  $H_{\text{rms}}$ .  $H_{\text{rms}}$  (1) and (2) decrease at the landward side of the top of the beachplain, whereas  $H_{\text{rms}}$  (3) remains of the same magnitude (Figure 29e). Dissipation across the beachplain is only caused by bed friction (Figure 29f&g). The  $k_s$  value of 0.25 m during high-energetic conditions, might be an overestimate of the actual storm conditions. When the  $k_s$  value is set to 0.05 m, the decrease in  $H_{\text{rms}}$  across the beachplain is less strong due to a decrease in  $D_{\text{bot,fr}}$  (not depicted).  $D_{\text{bot,fr}}$  decreases by approximately a factor 2 and  $D_{\text{br,fr}}$  remains zero. A smaller magnitude of  $k_s$  still shows a dominance of low-frequency wave dissipation due to bed friction at the Slufter.

The strong overestimation of the modelled  $H_{\text{rms}}$  for frequency range (1) and (3) might indicate that other dissipation mechanisms, such as wave-induced turbulence due to high-frequency wave breaking or nonlinear triad interactions in the inner surf zone which are not included in the model, may significantly contribute to low-frequency dissipation at the Slufter. The overestimation of the modelled  $H_{\text{rms}}$  occurs especially during high-energetic conditions, which make low-frequency wave dissipation due to wave-induced turbulence as a result of high-frequency wave breaking more likely than low-frequency wave dissipation due to nonlinear triad interactions. If nonlinear triad interactions would be a relevant mechanism of low-frequency wave dissipation, the modelled  $H_{\text{rms}}$  should also be overestimated in the surf zone during low-energetic conditions, which is not the case. However, no decisive conclusions concerning the contribution of the latter two low-frequency dissipation mechanisms at the Slufter can be drawn.

## 6. Conclusion

At the Slufter, high-frequency waves decrease in the surf zone whereas low-frequency waves propagate without dissipating which corresponds with findings from other studies (Guza & Thornton, 1985; Ruessink, 1998a; Karunarathna & Chadwick, 2007). Low-frequency waves become increasingly dominant over high-frequency waves with decreasing water depth and increasing offshore wave height. During low-energetic conditions, low-frequency waves dissipate in the swash zone for the upper low-frequency range (0.022-0.05 Hz). During high-energetic conditions, low-frequency waves dissipate at the landward side of the beachplain for the upper low-frequency range (0.011-0.05 Hz). Low-frequency wave dissipation is frequency dependant.

In the swash zone, low-frequency skewness and (negative) asymmetry increase with decreasing water depth in the swash zone during low-energetic conditions. During high-energetic conditions, low-frequency wave skewness and (negative) asymmetry increases on top of the beachplain. At the landward side of the beachplain, the shape of low-frequency waves becomes less skewed and asymmetric again. Low-frequency waves transform more strongly during low- than during high-energetic conditions due to smaller water depths present in the swash zone. The stronger transformation in wave shape during low-energetic conditions results in low-frequency shoaling and breaking, whereas during high-energetic conditions, low-frequency wave only shoal.

The cross-shore infragravity wave pattern at the Slufter is progressive and inundation of the beachplain does not have an effect on the cross-shore infragravity wave pattern. The progressive cross-shore infragravity wave pattern during normal beach conditions contrasts with findings from other studies (Guza & Thornton, 1985; Masselink, 1995; Henderson et al., 2001 and Sheremet et al., 2002) who found a (partial) cross-shore standing infragravity wave pattern. The difference in cross-shore structure is most likely related to a smaller beach slope present at the Slufter, resulting in low-frequency wave dissipation instead of reflection. Reflection at the shoreline is found to be small at the Slufter during normal beach conditions.

It is found that low-frequency wave dissipation is mostly caused by bed friction and to a lesser extent low-frequency wave breaking during low-energetic conditions. During high-energetic conditions, low-frequency wave dissipation is caused by bed friction. The role of low-frequency wave dissipation due to high-frequency wave-induced turbulence and nonlinear triad interactions in the surf zone is not analyzed. However, observations suggest

that high-frequency wave-induced turbulence may contribute significantly during more energetic conditions.

Surprisingly, the influence of the beachplain on infragravity wave behaviour at the Slufter is smaller than expected and infragravity wave behaviour is more strongly related to offshore wave height and water depth.

## References

- Aagaard, T., Bryan, K., 2003, *Observations of infragravity wave frequency selection*, Continental Shelf Research, vol. 23, pp 1019-1034
- Austin, M., Masselink, G., O'Hare, T., Russell, P., 2009, *Onshore sediment transport on a sandy beach under varied wave conditions: flow velocity skewness, wave asymmetry or bed ventilation?*, Marine Geology, vol. 259, pp 86-101
- Baldock, T.E., Huntley, D.A., Bird, P.A.D., O'Hare, T.O., Bullock, G.N., 2000, *Breakpoint generated surf beat induced by bichromatic wave groups*, Coastal Engineering, vol. 39, pp 213-242
- Battjes, J.A., Bakkenes, H.J., Janssen, T.T., Dongeren, A.R. van, 2004, *Shoaling of subharmonic gravity waves*, Journal of Geophysical Research, vol. 109, pp 1-15
- Bauer, B.O., Greenwood, B., 1990, *Modification of a linear bar-trough system by a standing edge wave*, Marine Geology, vol. 92, pp 177-204
- Berendsen, H.J.A., 2005, (in Dutch) *Landschappelijk Nederland*, pp 247, Van Gorcum & comp., Assen
- Butt, T., Russel, P., 1999, *Suspended sediment transport mechanisms in high-energy swash*, Marine Geology, vol. 161, pp 361-375
- Durieux, M.X., 2004, *De stabiliteit van de Slufter op Texel*, MSc thesis (unpublished)
- Dongeren, A. van, Battjes, J., Janssen, T., Noorloos, J. van, Steenhauer, K., Steenbergen, G., Reniers, A., 2007, *Shoaling and shoreline dissipation of low-frequency waves*, Journal of Geophysical Research, vol. 122, pp 1-15
- Elfrink, B., Baldock, T., 2002, *Hydrodynamics and sediment transport in the swash zone: a review and perspectives*, Coastal Engineering, vol. 45, pp 149-167
- Elgar, S., Guza, R.T., Raubenheimer, B., Herbers, T.H.C., Gallagher, E.L., 1997, *Spectral evolution of shoaling and breaking waves on a barred beach*, Journal of Geophysical Research, vol. 102, pp 15,797-15,805
- Foster, D.L., Guenther, R.A., Holman, R.A., 1999, *An analytic solution to the bottom wave boundary layer governing equation under arbitrary wave forcing*, Ocean Engineering, vol. 26, pp 595-623
- Guza, R.T., Thornton, E.B., 1985, *Observations of Surf Beat*, Journal of Geophysical Research, vol. 90, pp 3161-3172

- Henderson, S.M., Elgar, S., Bowen, A.J., 2001, *Observations of surf beat propagation and energetics*, (unpublished, but on the internet)
- Henderson, S.M., Bowen, A.J., 2002, *Observations of surf beat forcing and dissipation*, Journal of Geophysical Research, vol. 107, pp 1-10
- Henderson, S.M., Bowen, A.J., 2003, *Simulations of dissipative, shore-oblique infragravity waves*, Journal of Physical Oceanography, vol. 33, pp 1-12
- Henderson, S.M., Guza, R.T., Elgar, S., Herbers, T.H.C., Bowen, A.J., 2006, *Nonlinear generation and loss of infragravity wave energy*, Journal of Geophysical Research, vol. 111, pp 1-9
- Herbers, T.H.C., Elgar, S., Guza, R.T., 1995, *Generation and progradation of infragravity waves*, Journal of Geophysical Research, vol. 100, pp 24,863-24,872
- Heteren, S. Van, Oost, A.P., Spek, A.J.f. van der, Elias, E.P.L., 2006, *Island-terminus evolution related to changing ebb-tidal-delta configuration: Texel, The Netherlands*, Marine Geology, vol. 235, pp 19-33
- Karunaratna, H., Chadwick, A.J., 2007, *On low-frequency waves in the surf and swash zone*, Ocean Engineering, vol. 34, pp 2115-2123
- Klein Breteler, R., 2009, *Wave-induced sediment transport at the small tidal inlet 'Slufter' of Texel, the Netherlands*, MSc thesis (unpublished)
- List, J.H., 1991, *Wave groupiness variations in the nearshore*, Coastal Engineering, vol. 15, pp 475-496
- Löffler, M.A.M., Leeuw, C.C. de, Haaf, M.E. ten, Verbeek, S.K., Oost, A.P., Grootjans, A.P., Lammerts, E.J., Haring, R.M.K., (Het Tij Geleerd) guided by 'Expertteam Droge Wad', 2008, *Eilanden natuurlijk*, pp 95, Het Grafisch Huis, Groningen
- Longuet-Higgins, M.S., Stewart, R.W., 1962, *Radiation stress and mass transport in surface gravity waves in application to 'surf beats'*, Journal of Fluid Mechanics, vol 13, pp 481-504
- Madsen, P.A., Sørensen, O.R., Schäffer, H.A., 1997, *Surf zone dynamics simulated by a Boussinesq type model. Part 2: surf beat and swash oscillations for wave groups and irregular waves*, Coastal Engineering, vol. 32, pp 289-319
- Masselink, G., 1995, *Group bound long waves as a source of infragravity energy in the surf zone*, Continental Shelf Research, vol. 15, pp 1525-1547
- Masselink, G., Hughes, M.G., 2003, *Introduction to coastal processes and geomorphology*, pp 354, Hodder Arnold, UK

- Masselink, G., Kroon, A., Davidson-Arnott, R.G.D., 2006, *Morphodynamics of intertidal bars in wave-dominated coastal settings – A review*, *Geomorphology*, vol. 73, pp 33-49
- Price, T.D., Ruessink, B.G., 2008, *Morphodynamic zone variability on a microtidal barred beach*, *Marine Geology*, vol. 251, pp 98-109
- Raubenheimer, B., Guza, R.T., Elgar, S., 1996, *Wave transformation across the inner surf zone*, *Journal of Geophysical Research*, vol. 101, pp 25,589-25,597
- Raubenheimer, B., 2002, *Observations and predictions of fluid velocities in the surf and swash zones*, *Journal of Geophysical Research*, vol. 107, pp 1-7
- Rijn, L.C. van, Grasmeijer, B.T., Ruessink, B.G., 2002, *Accuracy of measurement instruments*, part of book *The behaviour of a straight sandy coast on the time scale of storms and seasons*, Aqua Publications, Amsterdam, the Netherlands
- Rijn, L.C., van (in pres), *Principles of fluid flow and surface waves in rivers, estuaries, seas and oceans*
- Rosales, P., Ocampo-Torres, F.J., Osuna, P., Monbaliu, J., Padilla-Hernández, R., 2008, *Wave-current interaction in coastal waters: Effects on the bottom shear stress*, *Journal of marine systems*, vol. 71, pp 131-148
- Ruessink, B.G., 1998a, *The temporal and spatial variability of infragravity energy in a barred nearshore zone*, *Continental Shelf Research*, vol. 18, pp 585-605
- Ruessink, B.G., 1998b, *Bound and free infragravity waves in the nearshore zone under breaking and nonbreaking conditions*, *Journal of Geophysical Research*, vol. 103, pp 12,795-12,905
- Sheremet, A., Guza, R.T., Elgar, S., Herbers, T.H.C., 2002, *Observations of nearshore infragravity waves: Seaward and shoreward propagating components*, *Journal of Geophysical Research*, vol. 107, pp, 1-10
- Symonds, G., Huntley, D.A., Bowen, A.J., 1982, *Two-dimensional Surf Beat: long wave generation by a time-varying breakpoint*, *Journal of Geophysical Research*, vol. 87, pp 492-498
- Thomson, J., Elgar, S., Raubenheimer, B., Herbers, T.H.C., Guza, R.T., 2006, *Tidal modulation of infragravity waves via nonlinear energy losses in the surfzone*, *Geophysical Research Letters*, vol. 33, pp 1-4